

Reliable computational prediction of supramolecular ordering of complex molecules under electrochemical conditions

Benedikt Hartl,[†] Shubham Sharma,[‡] Oliver Brügger,[‡] Stijn F. L. Mertens,^{¶,§}
Michael Walter,^{‡,||,⊥} and Gerhard Kahl[†]

[†]*Institute for Theoretical Physics and Center for Computational Materials Science (CMS),
TU Wien, Wien, Austria*

[‡]*FIT Freiburg Centre for Interactive Materials and Bioinspired Technologies,
Georges-Köhler-Allee 105, 79110 Freiburg, Germany*

[¶]*Department of Chemistry, Lancaster University, Lancaster LA1 4YB, United Kingdom*

[§]*Institute of Applied Physics, TU Wien, Wien, Austria*

^{||}*Cluster of Excellence livMatS @ FIT - Freiburg Center for Interactive Materials and
Bioinspired Technologies, University of Freiburg, Georges-Köhler-Allee 105, D-79110
Freiburg, Germany*

[⊥]*Fraunhofer IWM, MikroTribologie Centrum μ TC, Wöhlerstrasse 11, 79108 Freiburg,
Germany*

E-mail:

Abstract

We propose a computationally lean, two-stage approach that reliably predicts self-assembly behavior of complex charged molecules on a metallic surfaces under electrochemical conditions. Stage one uses *ab initio* simulations to provide reference data for

the energies (evaluated for archetypical configurations) to fit the parameters of a conceptually much simpler and computationally less expensive force field of the molecules: classical, spherical particles, representing the respective atomic entities; a flat and perfectly conducting wall represents the metallic surface. Stage two feeds the energies that emerge from this force field into highly efficient and reliable optimization techniques to identify via energy minimization the ordered ground state configurations of the molecules. We demonstrate the power of our approach by successfully reproducing, on a semi-quantitative level, the intricate supramolecular ordering observed experimentally for PQP⁺ and ClO₄⁻ molecules at an Au(111)-electrolyte interface, including the formation of open-porous, self-hosts-guest, and stratified bilayer phases as a function of the electric field at the solid-liquid interface. We also discuss the role of the perchlorate ions in the self-assembly process, whose positions could not be identified in the related experimental investigations.

May 4, 2020

1 Introduction

Supramolecular chemistry deals with intermolecular interactions and structure formation beyond individual molecules, and as such lies at the basis of many nano- and mesoscopic structures found in biology. In recent decades, impressive progress in the experimental branches of this field have resulted in at least two Nobel Prizes in chemistry. By contrast, the theoretical understanding and especially the *in silico* prediction of supramolecular ordering has lagged behind somewhat. This is easily understood if one considers the sheer size of the systems under study, requiring in many cases consideration of a solid substrate, a sufficiently large number of molecular building blocks or tectons, and a condensed matter medium (i.e. a solvent or electrolyte solution). The interaction of these three components, each with their intrinsic properties, and with optional extrinsic steering (e.g. by light, heat, electric field), will determine the observed supramolecular structures and govern the transitions between

them.^{1,2}

In this paper, we propose a new theoretical framework to predict supramolecular ordering of complex molecules at an electrochemical solid–liquid interface. The calculations were inspired by recent experimental work³ in which particularly clear-cut transitions between supramolecular structures were observed as a function of the applied electric field at a metal–electrolyte interface. The target molecules whose supramolecular ordering is considered constitute an organic salt that consists of a large, disc-shaped polyaromatic cation (PQP⁺) and a much smaller, inorganic anion (perchlorate, ClO₄⁻).^{4,5}

The concept of choice to investigate these scenarios would rely (i) on a faithful description of the properties of the system (notably a reliable evaluation of its energy) via *ab initio* simulations and (ii) in a subsequent step the identification of the optimized (ordered) arrangement of the molecules on the substrate by minimizing this energy via efficient and reliable numerical tools; this optimization has to be performed in a high dimensional search space, spanning all possible geometries of the unit cell and all possible coordinates and orientations of the molecules within that cell. Both these approaches, considered separately from each other, are conceptually highly complex and from the numerical point of view very expensive, which precludes the application of this combined concept even for a single set of external parameters (such as temperature, density, and external field); it is thus obvious that systematic investigations of the self-assembly scenarios of such systems are definitely out of reach.

In this contribution we propose an approach to overcome these limitations via the following strategy: in a first step we map the *ab initio* based energies onto the energy of a related classical model (or classical force field), where the atomistic units of the molecules are featured as spherical, charged units with Lennard-Jones type interactions and where the electrolyte is treated as a homogeneous, dielectric medium; the interaction between the atomic entities and the metallic surface is modelled by a classical, perfectly conductive, Lennard-Jones like wall potential. The as yet open parameters of the resulting force field

(energy- and length scales, charges, etc.) are fixed by matching the *ab initio* energies of the system with the related energies of this force field: this is achieved by considering archetypical configurations of the system’s building blocks (molecules and surface) and by systematically varying characteristic distances between these units over a representative range. These *ab initio* energies were then fitted along these ‘trajectories’ by the parameters of the classical force field: the energy- and length-scales of the involved interatomic Lennard-Jones or Mie potentials as well as the atom-wall interaction parameters.

It turns out that this force field is indeed able to reproduce the *ab initio* based energies along these ‘trajectories’ faithfully and with high accuracy. Even though the emerging force field is still quite complex (as it features both short-range as well as long-range Coulomb interactions and involves mirror charges) it is now amenable to the aforementioned optimization techniques which thus brings systematic investigations of the self-assembly scenarios of these molecules under the variations of external parameters within reach.

As a benchmark test for our approach we have considered the above mentioned system, studied in recent experimental investigations: the cation is PQP⁺ (9-phenylbenzo[1,2]quinolizino[3, 4, 5, 6-fed] phenanthridinylium, a disk-shaped polyaromatic molecule), while the anion is perchlorate, ClO₄⁻; the self-assembly of these ions on a Au(111) surface under the influence of an external electric field was studied. The high accuracy with which the ensuing energies calculated from the force field reproduce the *ab initio* simulation data make us confident about the applicability of the force field for the subsequent optimization step: using an optimization technique which is based on ideas of evolutionary algorithms we have then identified the self-assembly scenarios of the ions on the Au surface, for a given set of external parameters (temperature, density, and external field). These first results provide evidence that our approach is quite promising. This concept is furthermore completely flexible as it can easily be extended to other organic molecules of similar (or even higher) complexity. The computational cost of this optimization step is still substantial. Therefore we postpone a detailed, quantitative and, in particular, systematic investigation of the self-

assembly scenarios of the PQP^+ and the ClO_4^- ions on the Au surface for a broad range of external parameters to a later contribution. Instead we demonstrate in this contribution for selected sets of parameters that our approach is indeed able to reproduce several of the experimentally identified self-assembly scenarios.

In this context it has to be emphasized that such a type of optimization problem is highly non-trivial since the huge number of possible local minima in the potential energy surface (embedded in a high-dimensional parameter space) increases exponentially with the number of particles (and their degrees-of-freedom) of the system;⁶ thus exhaustive search strategies hit the computational limits or even exceed the capacities of present day supercomputers. Yet another complication in structure prediction algorithms is caused by the fact that different polymorphs of a system can be kinetically trapped and a vast number of other minima, having values of the internal energy comparable to the global minimum may also play an important role in structure formation processes.^{6,7}

At this point we owe an explanation to the reader why we have chosen the possibly unconventional approach. Of course, it is obvious that an optimization of the molecular configurations on the basis of full *ab initio* calculations is from the computational point of view by far out of reach. However, one can argue that suitable force fields (available in literature) or machine-learning (ML) potentials such as high-dimensional neural network potentials,⁸⁻¹⁴ kernel-based ML methods¹⁵ (such as Gaussian approximation potentials¹⁶⁻²⁰) or more specialized, effective potentials for selected molecular motives such as the SAMPLE approach^{7,21,22} might represent a more conventional approach to tackle this problem (note that the field of ML potentials is rapidly growing and the above list is far from comprehensive). Such arguments represent fully legitimate objections against our approach.

The problem we are addressing in this contribution is however a non-standard problem and thus requires to be treated with a custom force field: the justification for our strategy is that we wanted to endow the atomic units of the molecules with “real” physical properties (such as “size” or “charge”), which will help us to perform the second step in our structural

search that we have envisaged (and that we are currently working on): as the computational costs of our approach are still considerably, large scale investigations are still prohibitively expensive. In an effort to overcome these limitations we plan to proceed to even more coarse-grained models which grasp, nevertheless, the essential features of our complex molecules. On the basis of such models we would then be able to identify with rather low computational costs first trends in structural identification processes. Investigations along this direction will be explored in forthcoming contributions.

Finally we point out that we are well aware of the limitations and deficiencies of our present model. Features such as the response of the metallic electronic distribution of the gold surface due to the presence of an external bias, variable electrostatic properties of the molecular species (allowing thus for polarization effects), or a space dependent permittivity cannot be included in our concept. However, at this point it is fair to say that, to the best of our knowledge, none of the aforementioned alternative approaches (such as the use of conventional force fields or machine learning frameworks) are able to take all these effects faithfully into account, either.

The manuscript is organized as follows: In Section 2 we describe the essential features of the experimental setup, introduce an *ab initio* and a classical representation thereof and discuss the mapping procedure between those different instances. In Section 3 we put forward the memetic optimization procedure based on ideas of evolutionary algorithms in order to identify ordered ground state configurations of complex molecules under electrochemical conditions and in Section 4 we present selected numerical results which demonstrate a semi-quantitative agreement with the experimentally observed self-assembly scenarios of PQP^+ and ClO_4^- ions on an Au(111)-electrolyte-interface under the influence of an external electrostatic field. We conclude our findings in Section 5.

2 The system and its representations

2.1 The system

Both the DFT calculations and the related force field are based on a framework that mimics the essential features of the experimental setup, put forward (and discussed) in;³ this framework is schematically depicted in Fig. 1: PQP⁺ and ClO₄⁻ ions are immersed into an electrolyte (aqueous 0.1M perchloric acid). From below, the system is confined by a Au(111) surface, which in the experiment serves as the solid substrate for adsorption. An electric field, E_z , can be applied between a reference electrode located within the electrolyte and the Au surface. The PQP⁺ and the ClO₄⁻ ions are first treated via DFT based *ab initio* calculations (see Subsection 2.2). The calculated energies are then used to fix the force fields of classical particles (notably their sizes, energy parameters, and charges) which represent the atomic entities of the respective ions; the interaction between the atomic entities and the Au(111) substrate is described by means of a classical wall-particle force field (see Subsection 2.3). Throughout the electrolyte molecules are not considered explicitly. The electrolyte is rather assumed to be a homogeneous effective medium with a permittivity of water, i.e. $\epsilon_r = 78.36$, at $T = 25^\circ\text{C}$,²³⁻²⁵ corresponding to the temperature at which the experiments by Cui *et al.*³ were carried out and assuming that the low concentration of perchloric acid does not change the value of ϵ_r substantially.²⁶⁻²⁹ Hence, in this contribution we use ‘electrolyte’ as synonym for ‘solvent’ unless explicit use is required.

We emphasize at this point that in the experiment, an exact specification of the electric field strength is not possible: as detailed in the Supplementary Information of 3, the authors of the related experimental investigations have estimated rather the degree of charge compensation on the Au surface by the adsorbed PQP⁺ ions as a function of their changing coverage, which does not allow to estimate the electric field directly. This fact limits the degree of quantitative comparison between experiment and theory.

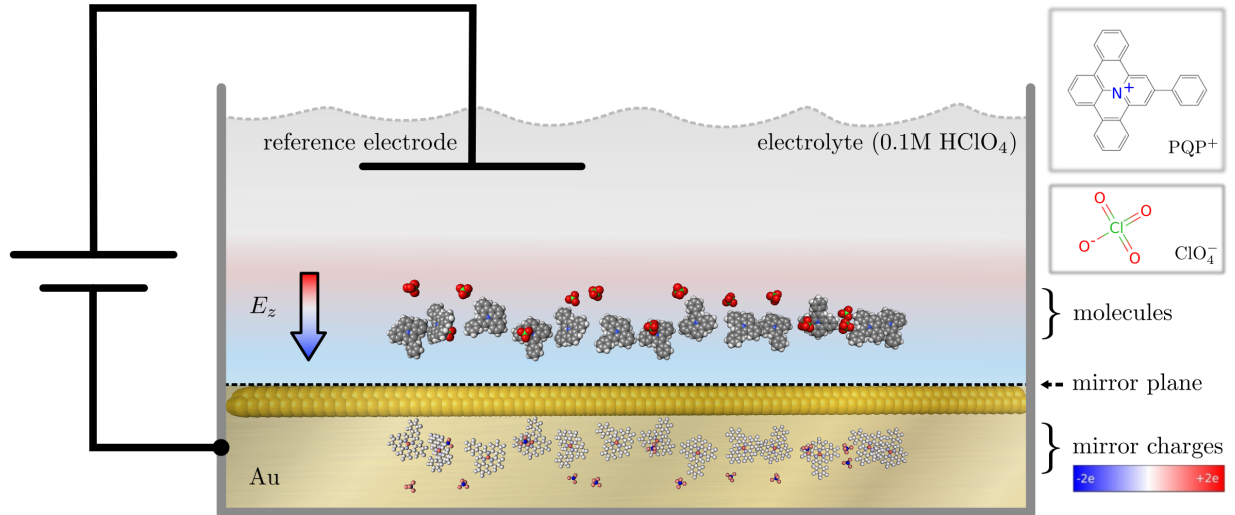


Figure 1: (color online) Schematic visualization of the experimental setup to control the pattern formation of PQP^+ (and ClO_4^-) molecules (structure formulas given in top right insets) close to a Au(111)-surface: two Au-layers are explicitly shown, the golden, shiny area represents the conductive Au-bulk, the black dashed line marks the surface of the electronic density which we interpret as mirror plane. The ions are immersed into an electrolyte (gray, shaded region), which is considered as an effective, homogeneous medium. In the region close to the Au surface (red to blue shaded areas) a homogeneous, electrostatic field E_z (bold, colored arrow), oriented in the z -direction, features the electrostatic potential drop between the Au-surface and the reference-electrode inside the electrolyte. The colors of the atoms in the electrolyte correspond to their type, while the color of the mirror-atoms (located in the Au-bulk) specify their partial charges, quantified by the colorbar (see bottom right) in units of the electron charge, e .

2.2 *Ab initio* simulations

The density functional theory calculations were performed with the software package GPAW^{30,31} and the structures handled by the atomic simulation environment.³² The electronic density and the Kohn-Sham orbitals were represented within the projector augmented wave method,³³ where the smooth parts were represented on real space grids with grid spacing of 0.2 Å for the orbitals and 0.1 Å for the electron density. The exchange-correlation energy is approximated as proposed by Perdew, Burke and Ernzerhof (PBE)³⁴ and weak interactions missing in the PBE functional are described as proposed by Tkatchenko and Scheffler (TS09).³⁵ The TS09 approximation assumes that long range dispersive contributions are absent in the PBE functional, such that these can be applied as a correction. The total energy which is written as

$$E = E_{\text{PBE}} + w_S E_{\text{vdW}} \tag{1}$$

where E_{PBE} is the PBE energy and E_{vdW} is the TS09 correction. We have introduced a weight factor w_S that will allow to incorporate electrolyte effects into the dispersive contributions as discussed below. For interactions in vacuum $w_S = 1$. The presence of the aqueous environment on the electronic and nuclear degrees of freedom included in E_{PBE} is modeled by a continuum solvent model.³⁶

Molecular interactions are studied on simulation grids with Dirichlet (zero) boundary conditions. Neumann (periodic) boundary conditions were applied in x - and y -directions in the surface plane for simulations involving the gold surface, while zero boundary conditions were applied in the perpendicular z -direction. The simulation grid was chosen such that at least 4 Å of space around the position of each atom in the non-periodic directions was ensured. The Au(111) gold substrate was modeled by two layers of 54 atoms, each using the experimental lattice constant of fcc gold of $a = 4.08$ Å. These settings result in a rectangular unit cell of 26.0×15.0 Å². The Brillouin zone was sampled by 3×3 Monkhorst-Pack³⁷

distributed k -points in the periodic directions.

Potentials are scanned by fixing all gold atoms and a central atom of PQP^+ (the nitrogen atom) and/or of ClO_4^- (the chlorine atom) to given positions while all other atoms were allowed to relax without any symmetry constraints until all forces were below $0.05 \text{ eV}/\text{\AA}$.

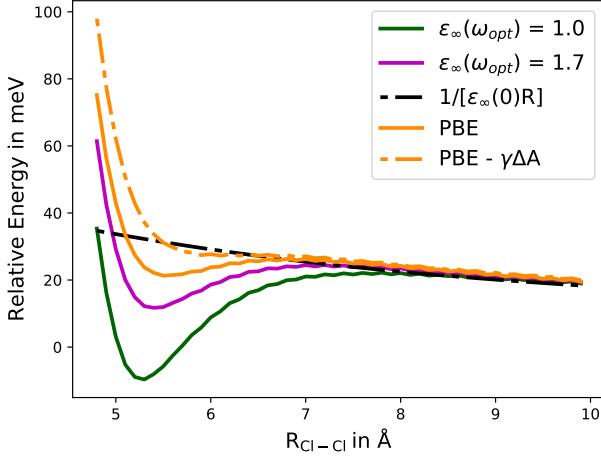


Figure 2: The relative energy of two ClO_4^- anions as a function of the distance between their chlorine atoms, $R_{\text{Cl-Cl}}$, where the separated anions define the energy reference; $\epsilon(\omega_{\text{opt}}) = 1$ with full van der Waals (vdW) corrections and $\epsilon(\omega_{\text{opt}}) = 1.7$ with scaled vdW corrections. The dash-dotted line shows the PBE energy where the energy contribution of effective surface tension $\gamma\Delta A$ is subtracted (see text).

The interaction of two perchlorate anions in dependence of their distance is shown in Fig. 2 for different approximations for the total energy in Eq. (1). As expected, the potentials follow the screened electrostatic repulsion $[\epsilon_\infty(0)R_{\text{Cl-Cl}}]^{-1}$ for large distances $R_{\text{Cl-Cl}}$, where $\epsilon_\infty(0) = \epsilon_r$ is the static relative permittivity of water. There is a slight attractive part in the potential around $R_{\text{Cl-Cl}} \simeq 5.2 \text{ \AA}$ already in the PBE potential which leads to a very shallow local minimum. The main reason for this minimum is the decrease in the effective surface ΔA when the solute cavities (the solvent excluded regions) begin to overlap. This decreases the energetic cost to form the surface due to the effective surface tension $\gamma = 18.4 \text{ dyn cm}^{-1}$ (γ also contains attractive contributions and is therefore much lower than the experimental surface tension of water³⁶). Subtracting $\gamma\Delta A$ nearly removes all of the minimum as demonstrated in Fig. 2. Including the full dispersion contribution $[\epsilon_\infty(\omega_{\text{opt}}) =$

1] this local minimum substantially deepens and becomes the total minimum of the potential. An attractive contribution to the potential is not to be expected for the interaction of two anions and needs further discussion. We suspect an overestimation of dispersion interactions if these are treated as in vacuum and no screening through the electrolyte is considered.

The aqueous environment influences the van der Waals (vdW) interactions as these are of Coulombic origin.³⁸ In order to derive an approximate expression for the screened vdW interaction of two molecules A and B at distance R inside the electrolyte, we express the C_6 coefficient defining the vdW energy C_6/R^6 by the Casimir-Polder integral^{35,39}

$$C_6 = \frac{3}{8\pi^2\epsilon_0} \int_0^\infty \alpha_A^*(i\xi)\alpha_B^*(i\xi)\phi(i\xi)d\xi \quad (2)$$

where $\alpha_{A,B}^*$ are the polarizabilities of the interacting molecules and ϕ is determined by propagation of the electric field through the embedding medium³⁹ with $\phi = 1$ in vacuum. Both $\alpha_{A,B}^*$ and ϕ are modified relative to vacuum in solution. In the simplest model³⁹ we may write $\phi(i\xi) = \epsilon_\infty^{-2}(i\xi)$ with the frequency dependent relative permittivity of the electrolyte ϵ_∞ . The effects of the electrolyte on the polarizabilities $\alpha_{A,B}^*$ should, at least partly, already be included in the TS09 description through the effective atomic polarizabilities derived from the self-consistent electron density calculated within the electrolyte. What is left is the effect of the permittivity entering through the function $\phi(i\xi)$ in Eq. (2). We assume that the main contribution of $\phi(i\xi)$ is at the resonance frequencies of α_{AB}^* , which are in the optical region for usual molecules. We further assume that $\epsilon_\infty(\omega_{\text{opt}})$ is approximately constant in this frequency region, such that we may pull $\phi = [\epsilon_\infty(\omega_{\text{opt}})]^{-2}$ out of the integral. This factor scales the C_6 coefficient and therefore the vdW contribution. In other words, we apply the weight $w_s = [\epsilon_\infty(\omega_{\text{opt}})]^{-2}$ in Eq. (2) with the experimental permittivity of water in the optical region of $\epsilon_\infty(\omega_{\text{opt}}) = 1.7$, see Ref. 40. This approach reduces considerably the depth of the suspiciously deep minimum as seen in Fig. 2 such that only a shallow local minimum remains similar to the PBE potential. The reduction obtained is quite strong in respect of the small

contributions of Axilrod-Teller-Muto interactions commonly assumed.^{41,42} The quantitative connection between the screening of dispersive interactions in polarizable media and the many-body effects neglected in TS09⁴³ are not immediately clear and is certainly worth further investigation. In what follows we use the same scaling for all the vdW contributions of the DFT potentials in this work.

2.3 Force field model

In this subsection we describe how we cast our setup into force fields where the atoms in the molecular constituents are described as spherical particles, each of them carrying a charge. The mapping is guided by the energies obtained via the *ab initio* simulations detailed above.

The Au(111) surface is modeled as a flat and perfectly conducting surface involving mirror charges as detailed below. However, we note, that the position of the corresponding surface in the DFT calculations does not coincide with the position of the atoms. Before proceeding the following comment is in order: in this mapping procedure the distance of a point charge to a metallic surface is unambiguously defined through the electrons leaking out of the potential defined by the nuclei.^{44,45} This feature can explicitly be seen in jellium models,⁴⁶ but emerges also in implicit calculations⁴⁷ where electrons spill out of the surface of metal clusters.⁴⁸ From the latter study we estimate an effective spill out of the surface of 0.5 Å, a value that agrees qualitatively with estimates from the jellium models, extrapolated to large structures.⁴⁵ This value will be used in the following for our problem.

2.3.1 The atomistic model

In our atomistic model the molecules are represented as rigid entities composed of atomistic constituents. The molecules are immersed into a microscopic electrolyte, which is treated as a continuous medium of given permittivity. From below the system is confined by a conducting Au(111)-surface (which is assumed to extend in the x - and y -directions), an external field (with respect to the electrolyte) can be applied in z -direction, i.e., perpendicular to the

surface (or wall). Fig. 1 schematically depicts all details of this atomistic model for the $\text{PQP}^+\text{ClO}_4^-$ system, confined by the Au-surface.

In order to specify the different entities of the system and their force fields we use the following notation:

- (i) Each of a total number of N molecules is uniquely labeled by capital Latin indices I : for each of these units this index is assigned to its center-of-mass (COM) position vector, \mathbf{R}_I , to a vector \mathbf{P}_I , specifying its orientation within the lab-frame in terms of the angle-axis framework^{49,50} (see S.I. Subsection 2.2 for more details), and to the set of coordinates, \mathbf{r}^{N_I} , of the respective N_I atomistic constituents of the molecule in its COM-frame (to which we also refer as its *blueprint*). The set of COM-positions and orientation-vectors of all N molecules are denoted by \mathbf{R}^N and \mathbf{P}^N . The set of all $n = \sum_{I=1}^N N_I$ atom positions in the lab-frame is given by \mathbf{r}^n , and the position of each atom in the lab-frame is uniquely defined by a vector \mathbf{r}_i , labeled with Latin indices ($i = 1, \dots, n$).
- (ii) Between all atoms we consider long-range Coulombic interactions (index 'C'),

$$U^{(C)}(r_{ij}) = \frac{1}{4\pi\epsilon_0\epsilon_r} \frac{q_i q_j}{r_{ij}} \quad i \neq j \quad (3)$$

with the inter-atomic distance $r_{ij} = |\mathbf{r}_i - \mathbf{r}_j|$ and charges q_i and q_j of the units i and j ; the dielectric constant ϵ_0 and the relative permittivity ϵ_r specify the implicit electrolyte. Further, we introduce short-range force fields (index 'sr') for which we have considered two options: first, a Lennard-Jones potential (index 'LJ'), i.e.,

$$U^{(LJ)}(r_{ij}) = 4\epsilon_{ij} \left[\left(\frac{\sigma_{ij}}{r_{ij}} \right)^{12} - \left(\frac{\sigma_{ij}}{r_{ij}} \right)^6 \right]; \quad (4)$$

for the energy- and length-parameters, ϵ_{ij} and σ_{ij} , we have opted for the standard Lorentz-Berthelot mixing rules,⁵¹ i.e., $\sigma_{ij} = \frac{1}{2}(\sigma_i + \sigma_j)$ and $\epsilon_{ij} = \sqrt{\epsilon_i \epsilon_j}$, respectively.

Alternatively, we have also considered for the short-range interactions the Mie potential⁵² (index 'Mie'), which can be considered as a generalization of the LJ interaction; its functional form is given by

$$U^{(\text{Mie})}(r_{ij}) = C_{ij}\epsilon_{ij} \left[\left(\frac{\sigma_{ij}}{r_{ij}} \right)^{\gamma_{ij}^{(R)}} - \left(\frac{\sigma_{ij}}{r_{ij}} \right)^{\gamma_{ij}^{(A)}} \right]; \quad (5)$$

and allows for a variation of the exponents of the repulsive and attractive contributions to the potential, $\gamma_{ij}^{(R)}$ and $\gamma_{ij}^{(A)}$, respectively. ϵ_{ij} and σ_{ij} are again parameters for the energy- and the length-scales. The C_{ij} are defined as functions of the exponents:⁵²

$$C_{ij} = \left(\frac{\gamma_{ij}^{(R)}}{\gamma_{ij}^{(R)} - \gamma_{ij}^{(A)}} \right) \left(\frac{\gamma_{ij}^{(R)}}{\gamma_{ij}^{(A)}} \right)^{\left(\frac{\gamma_{ij}^{(A)}}{\gamma_{ij}^{(R)} - \gamma_{ij}^{(A)}} \right)}; \quad (6)$$

for the exponents we apply arithmetic mixing laws, i.e., $\gamma_{ij}^{(R)} = \frac{1}{2}(\gamma_i^{(R)} + \gamma_j^{(R)})$ and $\gamma_{ij}^{(A)} = \frac{1}{2}(\gamma_i^{(A)} + \gamma_j^{(A)})$.

- (iii) We assume the Au-surface to be perfectly conductive, consequently we need to explicitly consider mirror-charges in our model; when further assuming $z = 0$ as the plane of reflection, the Coulombic interaction becomes

$$U'^{(C)}(r_{ij}) = U^{(C)}(r_{ij}) + U^{(C)}(r_{ij'}) + U^{(C)}(r_{i'j}) + U^{(C)}(r_{i'j'}) \quad (7)$$

with the mirror charges $q_{i'} = -q_i$ and their positions $\mathbf{r}_{i'} = (x_{i'}, y_{i'}, z_{i'}) = (x_i, y_i, -z_i)$.

- (iv) We describe the solid–liquid interface in terms of a slab-geometry with a lower confining wall, i.e., we assume periodicity in the x - and y -directions, but a finite extent, c_z , of the geometry in the z -direction which is chosen such that no restriction in the orientation of any molecule occurs, thus $c_z \approx 1.2 - 2$ nm, given their size and the slab-width. We define the (orthorhombic) lattice vectors, $\mathbf{a} = (a_x, 0, 0)$, $\mathbf{b} = (b_x, b_y, 0)$, and $\mathbf{c} = (0, 0, c_z)$, which, without loss of generality, define the volume of the unit-cell,

$V = a_x b_y c_z$, and which we collect within the matrix $\mathbb{V} = (\mathbf{a}, \mathbf{b}, \mathbf{c})$. Together with the molecular basis, given by \mathbf{R}^N , \mathbf{P}^N and all N (rigid) molecular blueprints, \mathbf{r}^{N_l} , we now define the supramolecular lattice

$$\mathcal{G} = \mathcal{G}(\mathbf{R}^N, \mathbf{P}^N, \mathbb{V}) = \{\mathbf{R}^N, \mathbf{P}^N, \mathbb{V}\}, \quad (8)$$

which gives rise to all atomic coordinates in the lab-frame, \mathbf{r}^n , i.e., the molecular crystal structure of the system (see S.I. Subsection 2.2).

- (v) The force field between the atomic entities and the Au-surface is described via a LJ-type wall potential,⁵³

$$U^{(\text{wall})}(z_i) = 2\pi\epsilon_{wi} \left[\frac{2}{5} \left(\frac{\sigma_{wi}}{z_i} \right)^{10} - \left(\frac{\sigma_{wi}}{z_i} \right)^4 - \frac{\sqrt{2}\sigma_{wi}^3}{3(z_i + (0.61/\sqrt{2})\sigma_{wi})^3} \right]; \quad (9)$$

in the above relation, z_i is the height of atom i above the surface, σ_{wi} and ϵ_{wi} are the length- and energy-parameters of the interactions of each atom i with the wall, respectively.

- (vi) Finally, we express the electrostatic interfacial potential between the electrode and the Au-surface by an external, homogeneous electrostatic field, E_z (i.e., oriented perpendicular to the surface): we account for this potential via $U^{(\text{field})}(z_i) = z_i q_i E_z$.⁵⁴

Thus and eventually the total potential energy of our model is given by the expression

$$U(\mathbf{r}^n, \mathbb{V}; E_z) = \sum_{i \neq j}^n [U^{(\text{C})}(r_{ij}) + U^{(\text{sr})}(r_{ij})] + \sum_{i=1}^n [U^{(\text{wall})}(z_i) + U^{(\text{field})}(z_i)], \quad (10)$$

with 'sr' standing for 'LJ' or 'Mie'; we recall that \mathbf{r}^n is the set of all n atomic positions \mathbf{r}_i in a lattice with slab-geometry (defined by the unit-cell \mathbb{V}). If not present (and not explicitly addressed) the electric field will be dropped in the argument list of Eq. (10), that is $U(\mathbf{r}^n, \mathbb{V}; E_z = 0) \equiv U(\mathbf{r}^n, \mathbb{V})$. The notation ' \sum^* ' indicates that summation is only carried

out over atoms, labeled with Latin indices i and j , which belong to different molecules I and J (with $I \neq J$); molecules being labeled with capital indices. The energy given in Eq. (10) and the corresponding force fields are efficiently evaluated using the software-package LAMMPS.⁵⁵

To evaluate the long-range Coulomb term, $\sum_{i \neq j}^n * U'^{(C)}(r_{ij})$ in the given slab-geometry we use numerically reliable and efficient slab-corrected 3D Ewald-summation techniques.^{56–58} The other terms in Eq. (10) are evaluated via direct lattice summation techniques.

2.3.2 Parametrizing the classical model via *ab-initio* calculations

In this work, the blueprint of each molecule \mathbf{r}^{N_I} is obtained from electronic structure calculations based on density functional theory (DFT), using dispersion corrected *ab initio* structure optimization,^{34,35} as described in Subsection 2.2. The partial charges of the atoms, q_i , are parametrized via a Bader analysis⁵⁹ and are collected in Tables 2 and 3 in the S.I. Subsection 2.3. These charges are directly transferred to the atomic entities. We repeat that throughout the electrolyte molecules have not been considered explicitly: instead, we treat within the force field the electrolyte as an effective, homogeneous medium, introducing the electric permittivity of water ϵ_r .

In order to fix the remaining model parameters that specify the interactions in Eq. (10) we search for each atomistic entity (labeled i) the set of atomistic model parameters (specified below) which reproduces via Eq. (10) the *ab initio* energies as good as possible. On one side we consider either the length- and the energy parameters of the LJ-potential (denoted by $\mathcal{L} = \{\sigma_i, \epsilon_i\}$) or the length- and the energy parameters together with the exponents of the Mie-potentials (denoted by $\mathcal{M} = \{\sigma_i, \epsilon_i, \gamma_i^{(R)}, \gamma_i^{(A)}\}$), as well as the wall parameters, $\mathcal{W} = \{\sigma_{wi}, \epsilon_{wi}\}$. To fix these parameters we proceed as follows:

- (i) We first perform *ab initio* structure optimization for different, characteristic molecular configurations, specified below. Here, molecules are either positioned next to each other (without considering the wall) or above the Au-surface: in the former case we fix

the positions of two selected atoms belonging to different molecules, the atoms being separated by r_{ij} ; in the latter case we keep the height, z_k , of one selected atom above the surface constant. Relaxation of all other degrees of freedom leads in the *ab initio* simulations to spatially and orientationally optimized molecular structures; they are denoted by $\mathbf{d}^n(r_{ij})$ and $\mathbf{d}^n(z_k)$, respectively, with corresponding energies $U_{\text{DFT}}(\mathbf{d}^n(r_{ij}), \mathbb{V})$ and $U_{\text{DFT}}^{(\text{wall})}(\mathbf{d}^n(z_k), \mathbb{V})$; they are, themselves, functions of the inter-atomic distance, r_{ij} , and the atom-wall separation, z_k , of the selected atoms.

- (ii) For every optimized *ab initio* structure, $\mathbf{d}^n(r_{ij})$ and $\mathbf{d}^n(z_k)$, obtained in this manner we define a corresponding molecular configuration $\mathbf{r}^n(r_{ij})$ and $\mathbf{r}^n(z_k)$, which is based on the above introduced rigid atomistic model \mathbf{r}^{N_I} (with the index I running now over all N molecules present in the respective DFT structure). To this end we synchronize the COM-positions of each molecule I in the *ab initio* simulation with the corresponding COM-positions \mathbf{R}_I of its classical counterparts and align their orientation \mathbf{P}_I accordingly.
- (iii) Finally we evaluate the corresponding energies with the help of the force field via Eq. (10) at zero electric field, i.e. $U_{\mathcal{L}/\mathcal{M}}(\mathbf{r}^n(r_{ij}), \mathbb{V})$ and $U_{\mathcal{L}/\mathcal{M},\mathcal{W}}^{(\text{wall})}(\mathbf{r}^n(z_k), \mathbb{V})$. We search for the best set of parameters \mathcal{L} (or \mathcal{M}) and \mathcal{W} via simultaneously minimizing

$$\mathcal{F}_{\mathcal{L}/\mathcal{M}} = \sum_{\{r_{ij}\}} \left| U_{\text{DFT}}(\mathbf{d}^n(r_{ij}), \mathbb{V}) - U_{\mathcal{L}/\mathcal{M}}(\mathbf{r}^n(r_{ij}), \mathbb{V}) \right|^2 \quad (11a)$$

$$\mathcal{F}_{\mathcal{L}/\mathcal{M},\mathcal{W}}^{(\text{wall})} = \sum_{\{z_k\}} \left| U_{\text{DFT}}^{(\text{wall})}(\mathbf{d}^n(z_k), \mathbb{V}) - U_{\mathcal{L}/\mathcal{M},\mathcal{W}}^{(\text{wall})}(\mathbf{r}^n(z_k), \mathbb{V}) \right|^2. \quad (11b)$$

Of course, in the model the same unit-cell, \mathbb{V} , and the same number of particles, n , as in the respective *ab initio* simulations have to be used. Note that in Eq. (11a) the wall-term included in Eq. (10) is obsolete since the surface atoms are not considered.

These fits are based on five particularly chosen, archetypical configurations, to be discussed in the following. In the panels of Fig. 3 we display schematic sketches of these configurations of the PQP^+ and ClO_4^- molecules; these panels show the corresponding energy curves obtained from the force field, with parameters based on a fitting procedure to the *ab initio* energy profiles.

- (a) *Tail-to-tail* configuration (see inset of in panel (a) in Fig. 3): We have considered a series of *ab initio* structure optimizations at constant, but successively increasing nitrogen-nitrogen distances, r_{NN} , in the x -direction (while keeping y_{NN} and z_{NN} constant) of an anti-parallel oriented pair of PQP^+ molecules; both cations are vertically decorated with a ClO_4^- molecule. The aromatic parts of the PQP^+ molecules lie flat in the x - and y -directions such that their tails face each other.
- (b) *Face-to-face* configuration (see inset in panel (b) in Fig. 3): In this case we consider anti-parallel oriented, but vertically stacked PQP^+ molecules (both being horizontally decorated by ClO_4^- molecules) under the variation of the nitrogen-nitrogen distance, r_{NN} , in z -direction (while now keeping x_{NN} and y_{NN} constant). Again, the aromatic parts of the PQP^+ molecules lie flat in x - and y -directions; however, and in contrast to case (a) these units face each other.
- (c) $\text{ClO}_4^- - \text{ClO}_4^-$ configuration (see inset in panel (c) in Fig. 3): Here two ClO_4^- molecules are considered, varying the chlorine-chlorine x -distance, r_{ClCl} , while keeping y_{ClCl} and z_{ClCl} constant.
- (d) *Face-to-wall topped* configuration (see inset in panel (d) in Fig. 3): In this case a single PQP^+ molecule, lying flat and parallel to the (x, y) -plane, is located above two layers of Au and is vertically decorated by a ClO_4^- molecule. The cell geometry is assumed to be periodic in the x - and y -directions and finite along the z -axis; in an effort to scan along the z -direction, we have performed a series of *ab initio* based structure optimizations for selected fixed values of z_{N} , i.e., the z -position of the nitrogen in PQP^+ above the

Au-surface. The LJ 10-4-3 potential⁵³ has been used between the Au(111) surface and the molecules.

- (e) *Face-to-wall beside* configuration (see inset in panel (e) in Fig. 3): In contrast to case (d), the PQP⁺ cation is now horizontally decorated by the ClO₄⁻ anion such that both molecules are adsorbed on the Au-surface. Again, the LJ 10-4-3 potential⁵³ has been used between the Au(111) surface and the molecules.

In practice we first optimize $\mathcal{F}_{\mathcal{L}/\mathcal{M}}$, given in Eq. (11a), involving thereby *all* inter-atomic force field parameters; their values are listed in Table 1 for the LJ and the Mie models. These parameters are then kept fixed and are used in the subsequent calculations to optimize the wall force field parameters via optimizing $\mathcal{F}_{\mathcal{L}/\mathcal{M},\mathcal{W}}^{(\text{wall})}$, specified in Eq. (11b); the emerging parameters are listed in Table 2. In panel (f) of Fig. 3 we present a visualization of the molecules PQP⁺ and ClO₄⁻, using these optimized parameters and providing information about the charge of the atomic entities via the color code.

3 Identifications of self-assembly scenarios

With the classical force field for the PQP⁺ and ClO₄⁻ molecules introduced in Subsection 2.3.1 at hand we are now ready to identify the ordered ground-state configurations of these molecules as they self-assemble on the Au-surface – immersed into an electrolyte and exposed to an electric field. While we leave a more comprehensive and systematic investigation of these self-assembly scenarios to a future publication,⁶⁰ we focus in this contribution on the technical details of our approach and on a few selected sets of external parameters (i.e, the electric field strength and the particle density).

Our overall objective is to find for our system the global minimum of the total free energy, F , at $T = 0$ K as a function of the positions and orientations of all molecules per unit-cell for a given value of cell volume and E_z ; at $T = 0$ this task reduces to the minimization of the internal energy U . The minimum has to be found in a huge-dimensional parameter space,

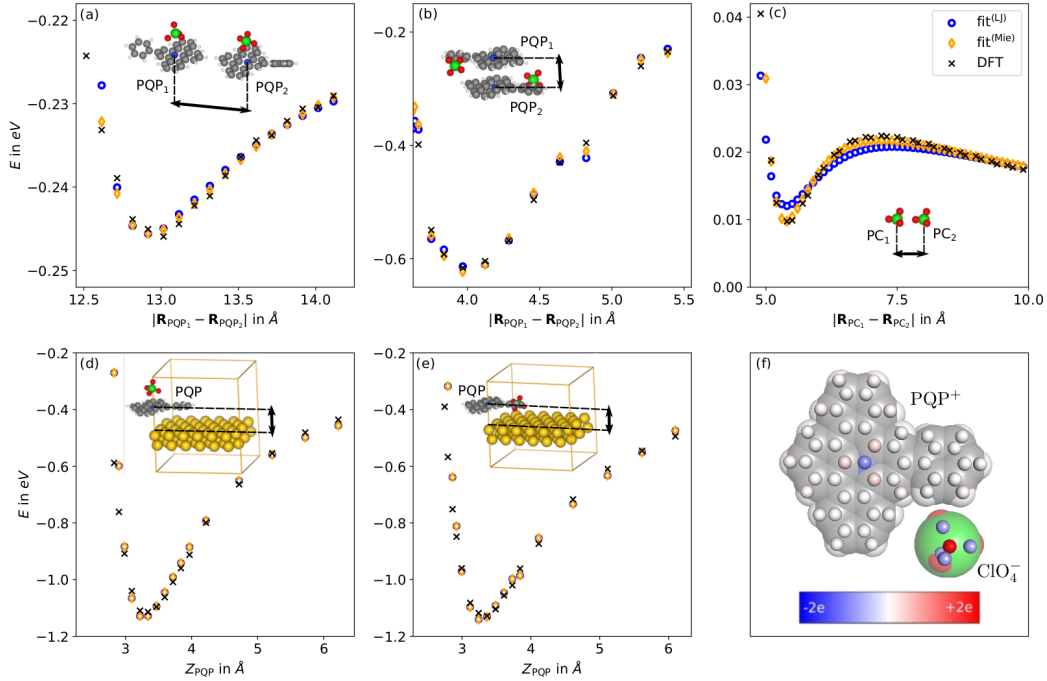


Figure 3: (color online) Energies as obtained in *ab initio* simulations (black crosses) and fitted data, using the force field (involving a LJ interactions – open blue circles – or Mie interactions – open orange diamonds), see Subsection 2.3.1; also shown are – with labels (a) to (e) – five schematic sketches of the five archetypical configurations of the molecules (along with their relative displacements, schematically indicated via the arrows as the distances vary along the abscissa); the related energy curves are used to fit the parameters of the force field, as outlined in the text; the labels correspond to the itemization (a) to (e) used in Subsection 2.3.2. Panel (f): PQP⁺ and the ClO₄⁻ molecules, drawn to scale and using the Mie force field for the short-range interactions: atomic entities are shown as transparent spheres with their diameters fixed by their respective optimized σ_i -values and their Bader charges (see color code).

spanning the positions and orientations of the molecules and by the parameters specifying the unit cell. To be more specific, the dimensionality is set by the number of parameters to be optimized, which read 64, 76, and 88 for five, six, and seven molecules per unit cell, respectively. It is a particular strength of our optimization algorithm (as detailed in the following) to identify in an efficient and reliable manner minima in such high dimensional search spaces.

For this purpose we use a memetic search algorithm which combines evolutionary search strategies (EA)⁶¹⁻⁶⁷ and local, steepest gradient descent procedures (LG):^{68,69} First a total number of N_{EA} different lattice-configurations, $\mathcal{G} = \mathcal{G}(\mathbf{R}^N, \mathbf{P}^N, \mathbb{V})$ as defined in Eq. (8), is generated. We note that among those configurations we have also intentionally included as “educated guesses” molecular configurations, inspired by the experimental self-assembly scenarios identified in Ref. 3; however it should be emphasized that this information is only available for the PQP⁺ ions, as the experiment does not provides any information about the positions of the perchlorate ions. This *population*, $\mathcal{G}^{N_{\text{EA}}}$, is exposed to concepts of natural (or, rather, artificial) selection. At every iteration step of the EA a new configuration, i.e. an *offspring*, is created from existing configurations of the most recent population, via crossover and mutation operation. This new configuration is then subjected to an LG optimization, an operation which represents by far the most time consuming task in our algorithm and is performed in parallel using the “*mpi4py*“ framework.⁷⁰⁻⁷² For an optimal load-balance we additionally spawn a master-thread on one of the mpi-processes to asynchronously distribute optimization tasks of offspring configurations among all idle mpi-processes. The relaxed configurations are gathered by this master-thread, which then decides – via a criterion primarily based on the respective internal energy of the configurations – whether the new relaxed particle arrangements are accepted or rejected.

Since the experimental observations^{3,5} provide evidence of a structural organization of the molecules into supramolecular lattices, the center-of-mass coordinates of the molecules, \mathbf{R}^N , and their orientations, \mathbf{P}^N , as well as the parameters defining the unit-cell, \mathbb{V} , (see

Subsection 2.3.1 and Fig. 1 for details), are the variables which have to be optimized for the search of ground-state configurations: We minimize $U(\mathbf{r}^n, \mathbb{V}; E_z)$, defined in Eq. (10), with respect to \mathbf{R}^N , \mathbf{P}^N , and \mathbb{V} , keeping the number of molecules N , the unit-cell volume V (with fixed slab width c_z), and the electrostatic field strength E_z constant.

In more detail, we proceed as follows:

- (i) It is common in evolutionary algorithms to define a genome representation of the entity which is subject to optimization.^{73,74} In our case we represent a supramolecular lattice configuration phenotypically (rather than genotypically⁷⁴) by the set, $\mathcal{G} = \{\mathbf{R}^N, \mathbf{P}^N, \mathbb{V}\}$ as defined by Eq. (8), i.e. the set of all COM coordinates and orientations of all molecules as well as the lattice vectors.
- (ii) In the first step, two configurations (labeled henceforward by Latin indices), \mathcal{G}_i and \mathcal{G}_j , are chosen at random or via the "roulette wheel" method (see item (v) below) from the evolutionary population;^{61,62,75-77} this strategy favors parents of high quality hence making them more likely to be used for reproduction than "weaker" configurations, i.e. configurations with higher energy from the evolutionary population. Then these two configurations are combined via a crossover operation (i.e., a cut-and-splice process – for more details see below) creating thereby an offspring configuration, $\mathcal{G}_{i\oplus j}$, with the subscript ' $i \oplus j$ ' emphasizing the executed crossover operation between \mathcal{G}_i and \mathcal{G}_j . supramolecular lattice. The purpose of this operation is to save high quality blocks of the genetic material (e.g. the relative positions and orientations of molecules within the unit-cell) in order to efficiently sample the parameter space.^{61,62,73-77}
- (iii) In the second step, the newly generated offspring configuration, $\mathcal{G}_{i\oplus j}$, is then exposed to random mutation moves: these are either translations or rotations of single molecules, swaps of center-of-mass positions or orientations of pairs of molecules or deformations of the unit-cell, each of them with a certain probability and within preset numerical boundaries. This step of the algorithm has the purpose of exploring disconnected areas

in parameter space, a feature which is indispensable in global minimization techniques.

(iv) After these two steps, and assuming that the offspring configuration, $\mathcal{G}_{i\oplus j}$, does not represent a local minimum with respect to the potential energy, a local energy minimization is performed. Here we mainly rely on the “*scipy*” implementation of the *SLSQP* gradient-descent algorithm^{68,69} (allowing us to define numerical boundaries and constraints on the parameters during the optimization), which minimizes the forces and torques between the molecules as well as the stress of the unit-cell. These tools are very helpful to keep the unit-cell volume fixed and to prevent re-orientations of the molecules where some of their atomic constituents would be transferred into positions outside the slab geometry, ensuring thus that $z_i > 0$ for all atoms. Subsequently we perform several “basin-dropping“ (BD) steps, where we further try to lower the energy of the configuration by applying several small random “moves“ in the parameter space of the LG-optimized offspring; from the emerging configurations only the ones with low energies are accepted. This specific operation turned out to considerably improve the convergence rate of the local optimization, in particular if multiple and alternating sequences of LG and BD runs are applied.

(v) After the local search procedure the optimized offspring configuration, $\mathcal{G}_{i\oplus j}$, becomes a new candidate to enter the evolutionary population, \mathcal{G}^{NEA} . The objective of the EA is to retain the best configurations (i.e., the energetically most favorable ones) within the population and to include only candidates with energy values better or comparable to those of the current population. In an effort to quantify the quality of the candidates, their so-called fitness is evaluated,^{61,62,74-77} for which we have used in this contribution the function:

$$F(U) = \exp\left(-s \frac{U - U_{\min}}{U_{\max} - U_{\min}}\right); \quad (12)$$

$F(U)$ is a monotonic function of the energy U of the candidates, whose value ranges

within the interval $0 \leq F(U) \leq F(U_{\min}) = 1$; U_{\min} and U_{\max} are the minimal and maximal energies appearing in the population. The selection parameter s quantifies the reproduction-rate for configurations within the population in the sense that large values of s tend to exclude configurations with low fitness from reproduction; following⁷⁷ we commonly use $s = 3$. The aforementioned “roulette wheel” method for choosing suitable parent configurations also relies on the fitness function (and hence the selection parameter): Assuming that the configurations within the population $\mathcal{G}^{N_{\text{EA}}}$ are sorted by their respective fitness values in descending order, $F(U_i) > F(U_{i+1})$, the probability, $f(U_i)$, of a configuration, \mathcal{G}_i , to be selected for reproduction is given in terms of the relative fitness:^{61,75–77}

$$f(U_i) = \sum_{j=i}^{N_{\text{EA}}} F(U_j) \cdot \left[\sum_{k=1}^{N_{\text{EA}}} \sum_{j=k}^{N_{\text{EA}}} F(U_j) \right]^{-1}, \quad (13)$$

N_{EA} being the total number of configurations within the population. With a certain probability (commonly in 20% of all crossover moves) we allow reproduction between randomly chosen configurations.

- (vi) Once a new configuration is accepted to enter the population another configuration has to be eliminated. The probability $p(U_i)$ for a configuration, \mathcal{G}_i , to be replaced is given by

$$p(U_i) = \exp[-sF(U_i)] \left[\sum_{j=1}^{N_{\text{EA}}} \exp[-sF(U_j)] \right]^{-1}, \quad (14)$$

a value which is again related to the fitness of the configuration, $F(U_i)$, and the selection parameter s . Thus, configurations with low fitness are more likely to be eliminated. In any case, a few of the best configurations within the population are retained in an effort to keep the so far best solutions as appropriate parent candidates for the above-mentioned crossover procedures (a strategy referred to in the literature as *elitism*⁷⁵).

It should be emphasized that this strategy does not follow biological selection mechanisms,⁷⁸ where populations are replaced entirely once that new generations have been formed; however, our strategy ensures to protect the best genetic material from extinction during the entire search procedure.^{75,77}

- (vii) In an effort to maintain diversity within the population an additional operation (in literature referred to as *nichening*^{79,80}), is applied: locally optimized offspring configurations will be discarded if the values of their energy is too close to the energy of any configuration currently in the population; avoiding thereby that the population is overrun by structurally identical configurations. At the same time the maintenance of genetic diversity is guaranteed.

However, this procedure alone cannot cope with 'degenerate' configurations, i.e., if structurally distinct configurations have essentially the same energy values (within the specified nichening tolerance). In our approach we allow configurations to enter the population only if their structures differ significantly from those of the competing, degenerate configurations. In order to quantify the structural difference between configurations we associate a feature vector, \mathbf{f}_i (i.e. a set of order parameters), which collects a set of order parameters pertaining to configuration \mathcal{G}_i (see S.I. Subsection 3.2 for details). The degree of similarity between two configurations, \mathcal{G}_i and \mathcal{G}_j , is then evaluated by taking the Euclidean distance between the corresponding feature vectors, i.e., $\Delta_{ij} = |\mathbf{f}_i - \mathbf{f}_j|$; similar configurations will have a small distance, while unlike configurations will have a large distance. If Δ_{ij} is above a certain threshold value, the offspring configuration, $\mathcal{G}_{i\oplus j}$, will not be discarded by the energy-nichening operation.

In order to offer the reader an insight into the computational complexity of our project we outline via a few characteristic numbers the computational limitations: the bottleneck of the identifications of self-assembly scenarios are (i) the huge number of calls of energy-evaluations in the optimization step, as underlined via some example: per generation we have

at least 10^4 calls of the energy kernel; for each state point we need at least 10^4 generations, which leads to an absolute minimum of 10^8 calls of the energy kernel for *one (!)* set of system parameters; (ii) the optimization of the energy in a high dimensional search space (as specified above), ranging from ~ 60 to 90, depending on the number of molecules.

Summarizing, the complexity of the problem at hand forces us to use all the above listed advanced optimization tools, including a basin hopping memetic approach combining the heuristic nature of evolutionary strategies with deterministic local gradient descent algorithms.⁶¹ The gradient descent method deterministically evaluates every local minimum of the basin with high accuracy (which is additionally sped up by the "basin dropping" procedure) while the evolutionary search gradually adapts its population to the energetically most favorable solution, exploring the search space for the global optimum.

To round up this section it should be noted that a variety of techniques have been used in literature for related optimization problems; among those are: Monte Carlo or molecular dynamics-based techniques such as simulated annealing,^{81,82} basin-hopping,⁸³⁻⁸⁵ minima hopping,^{86,87} and eventually evolutionary approaches such as genetic algorithms.^{61-67,79,80,88-91} The decision on the method of choice relies on the specific problem: for instance, as Hofmann *et al.* used the SAMPLE technique (see Refs. 7,21,22), relying on a discretization of the search space into limited, archetypical, intermolecular motives and elaborate data fitting of emerging force fields to describe intermolecular interactions. To the best of our knowledge, this approach has neither been applied to molecular motives beyond monolayer configurations or to charged molecules, so far, nor has it been used in combination with an external control parameter, such as an electric field or systems composed of multiple components. In general, the fact that the number of archetypical inter-molecular motives grows rapidly with the increasing size of the molecules bears the risk of hitting very soon the limits of computational feasibility. However, suitable adaptations of this strategy and/or a combination with evolutionary search strategies or with reinforcement learning – which has, for instance, very successfully been applied to protein folding problems⁹² in a similar way as AlphaGo⁹³

was able to master the infamous board game – might represent a viable route to circumvent the aforementioned limitations; thus future investigations of such intricate problems as the complex monolayer to bilayer transition, addressed in this contribution, might come within reach.

4 Results

4.1 General remarks and system parameters

In the following we present selected results for self-assembly scenarios of PQP^+ and ClO_4^- molecules on an Au(111)-electrolyte-interface under the influence of an external electrostatic field, as obtained via the algorithm presented in the preceding sections. Our choice of parameters is guided by the experimentally observed molecular configurations.³ We demonstrate that our proposed strategy is indeed able to reproduce on a semi-quantitative level the experimentally observed self-assembly scenarios.³ As a consequence of the still sizable costs of the numerical calculations we leave more detailed investigations (where we systematically vary the system parameters) and a quantitative comparison of our results with the related experimental findings³ to a future contribution.⁶⁰

To be more specific we have used the following values for the (external) system parameters:

- an indication for the number of molecules per unit cell is provided by the experiment:³ we have considered unit cells containing ten, twelve, and 14 pairs of PQP^+ and ClO_4^- molecules. These numbers in molecules include, of course, also the related mirror molecules and correspond to 630, 636, and 742 atomic entities per unit cell, respectively (which interact via short-range and long-range potentials, which are subject to particle wall interaction and which are sensitive to an external electrostatic field);
- also the actual values of the surface area A is motivated by estimates taken from

experiment:³ we have varied A within the range of 6.5 nm^2 to 12.25 nm^2 , assuming a step size of typically 0.5 nm^2 ; systems will be characterized by the surface density of the PQP^+ molecules, defined as $\sigma_{\text{PQP}} = N_{\text{PQP}}/A$, N_{PQP} being the number of PQP molecules per unit cell;

- the range of the experimentally realized values for the electrostatic field strength E_z is, however, difficult to estimate since the major drop in voltage occurs near the negatively charged Au-surface and the nearby layers of cations,⁵⁴ which is not directly accessible in experiment. Therefore we have covered – at least in this first contribution – several orders of magnitude in the value for E_z within a range that extends (on a logarithmic grid) from $E_z = -1 \text{ V/nm}$ to $E_z = -10^{-3} \text{ V/nm}$; in addition, we have also performed calculations at zero electrostatic field.

It should be mentioned that we have used in all these calculations the Mie potential within the classical model, since the related LJ model is not able to fit the *ab initio* data with a comparable and sufficient accuracy (see also discussion in Subsection 2.3.1).

We have covered in total approximately 176 combinations of these parameters (that is the unit-cell volume V with a constant slab width c_z , the number of molecules N , and the electrostatic field strength E_z); for each of these we performed independent evolutionary searches with a population size of typically $\mathcal{G}^{\text{NEA}} = 40$ configurations. Some details about the numerical costs of our calculations can be found in S.I. Subsection 4.1

4.2 Discussion of the results

4.2.1 Lateral particle arrangements

In this subsection we discuss the lateral self-assembly scenarios of the PQP^+ and of the ClO_4^- molecules. Selected results for our numerical investigations are presented in Fig. 4 and in – on a more quantitative level – in Table 3. The actual values have been chosen in an effort to reproduce – at least on a qualitative level – the results obtained in the experimental inves-

tigations. Indeed, the sequence of the obtained ordered ground state configurations (shown in panels (a) to (c)) clearly indicates the transition from a stratified bilayer configuration (identified at a rather strong electrostatic field strength of $E_z = -0.3$ V/nm), over a self-hosts-guest mono-layer structure (obtained by reducing the field down to $E_z = -0.1$ V/nm), and eventually to an open-porous configuration (identified at $E_z = -0.01$); similar observations have been reported in the related experimental study.³

From the results of our investigations (which are shown only selectively) we learn that an electrostatic field strength of $E_z = -0.3$ V/nm always leads to bilayer configurations, similar to the one shown in panel (a) of Fig. 4. This stratified bilayer configuration represents the energetically most favorable one as we vary at fixed E_z the volume of the unit cell and the number of molecules within the respective ranges, specified in the preceding section; the numerical data of the related internal energy are compiled in Table 3.

As we proceed to $E_z = -0.1$ V/nm we observe self-assembly scenarios as the ones depicted in panels (b) and (d) of Fig. 4, which correspond to self-hosts-guest configurations observed in experiment;³ for the data presented in these panels two different values for N_{PQP} (and hence for σ_{PQP}) have been considered: the mono-layer configuration shown in panel (b) has a slightly better value for the internal energy (per molecule) than the rhombohedral bilayer configuration shown in panel (d); however, as can be seen from Table 3 the energy differences are very tiny: differences of the order of 10^{-4} eV correspond to values where we hit the numerical accuracy of the *ab initio* based energy values).

Eventually, we arrive at the so-called open-porous structures, observed in experiment:³ the ground state configurations depicted in panels (c), (e), and (f) of Fig. 4 are evaluated at the same electrostatic field strength of $E_z = -0.01$ V/nm, assuming different values for N_{PQP} and σ_{PQP} ; the open-porous pattern emerging in panels (c) is the most favorable one in terms of energy per molecule (see Table 3 for the numerical details). There are, however, several serious competing structures with minute energy differences at this value of the electric field strength: another open-porous structure, depicted in panel (f), with an energy penalty of

less than 8.1 meV per PQP⁺ molecule compared to case (c) and also a considerably denser configuration, depicted in panel (e), with an internal energy value worse by only 11.3 meV compared to case (c) and by 3.2 meV compared to case (f).

From the numerical point of view the following comments are in order: for a fixed state point, the energy differences of competing structures attain values which hit the limits of the accuracy of the *ab initio* based simulations, which can be estimated to be of the order of 0.1 eV to 0.01 eV per molecule for dispersive interactions.^{35,94–96} These values set the limits of our numerical accuracy. For completeness we note that for the results for the energies obtained via the classical force field (which are based on LAMMPS calculations) we estimate that our results are numerically reliable down to $\sim 10^{-6}$ per atom; within the range of such minute energy differences no competing structures have been found in our investigations. In general we observe that the energy differences for the energetically optimal ground state configurations become smaller as the electrostatic field tends towards zero. Even though the optimization algorithm (as outlined in Section 3) has turned out to be very efficient and reliable, we observe (in particular for smaller values of the external field) that new configurations are included in the population of the best individuals even after a large number of optimization steps.

4.2.2 Vertical particle arrangements

In Fig. 5 we present in separate panels the height distributions of PQP⁺ and ClO₄⁻ as functions of the electrostatic field, E_z (which is binned for the six different values of E_z that were investigated); along the vertical axis we count (for a given value of E_z) the occurrence of the respective molecules in bins of one Å, considering all configurations identified by the evolutionary algorithm, which are located within an interval of at most 1k_BT (or 43 meV) above the configuration with the best energy, which are of the same order of magnitude as the values presented in Table 3 for different electric field strengths, E_z ; these distributions are generated by counting, at a given value of E_z , the vertical occurrence of the respective

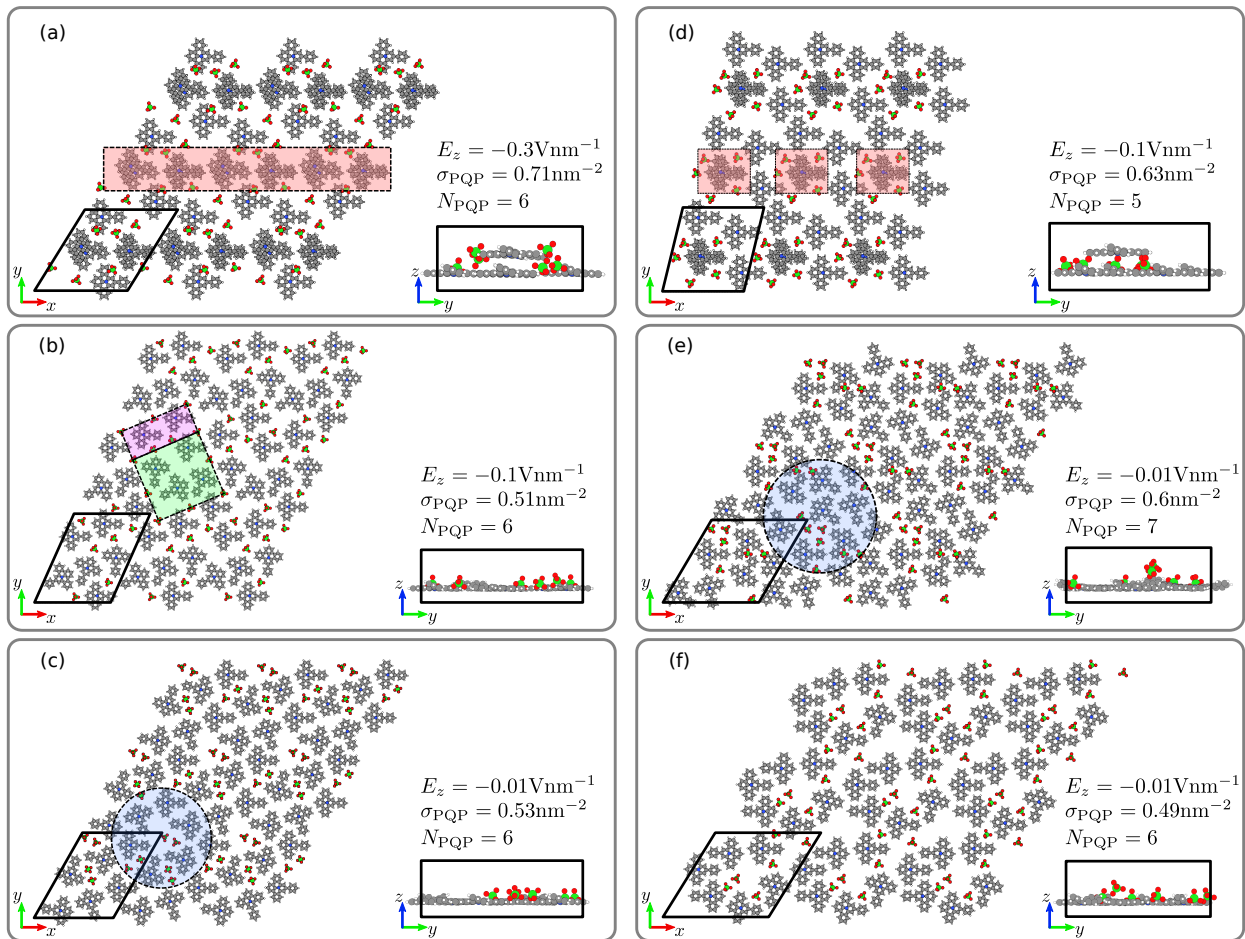


Figure 4: (color online) Results for the ground state configurations of PQP^+ and ClO_4^- molecules, adsorbed on a Au(111) surface under the influence of an external electrostatic field E_z , as they are obtained via the numerical procedure, as specified in Section 3; calculations are based on the classical model for the molecules, involving the Mie potential (for details see Subsection 2.3.1). In the main panels configurations are shown in a periodically extended view as projections onto the (x, y) -plane and in the respective insets as projections onto the (y, z) -plane; in the main panels the respective unit cells are highlighted by thick black lines. Results are shown for different values of the number of PQP molecules, the surface density σ_{PQP} and the electrostatic field E_z : see labels in the different panels and Tab. 3 for details. The red (gray) shaded areas, framed with dashed lines, in panel (a) and (d) emphasize PQP^+ molecules which sit on top of other cations, forming a bilayer structure. The dashed, shaded, magenta (gray) rectangular and green (gray) square areas in panel (b) represent tilings formed by perchlorate molecules within the dense PQP^+ monolayer configuration. The dashed, shaded, blue (gray) circles in panel (c) and (e) emphasize, quantitatively, the porous and auto-host-guest tiles identified in experiment (see Fig. 4A and Fig. 4C in Ref. 3, respectively).

molecules in bins of one Å, and are normalized by the total number of encountered structures. Note in this context that the distance of the first layer of PQP⁺ molecules can be directly estimated by the vertical equilibrium position of carbon atoms, $z_C^{(\text{eq})} = 3.166\text{Å}$, obtained by minimizing Eq. (9) for a single carbon atom with $\sigma_{\text{wC}}^{(\text{Mie})} = 3.208$, taken from Table 2.

For the high values of the field strength (i.e. for $E_z = -10\text{ V/nm}$ and -1 V/nm) the PQP⁺ ions are preferentially adsorbed onto the gold surface as a closely packed monolayer (see left panel of Fig. 5), while the perchlorate anions are strongly dissociated and assemble as far from the gold surface as possible (corresponding in our investigation to the numerical value of the slab height, which we fixed to 12 Å) – see right panel in Fig. 5. This situation represents an extreme case in the sense that neither the Coulomb nor the short-range Mie interactions between ions and anions can compensate for the strong negative surface potential.

Decreasing now the magnitude of the electrostatic field to the more moderate value of $E_z \sim -0.3\text{ V/nm}$ reveals the emergence of a bilayer structure, formed by the PQP⁺ molecules, with pronounced peaks located at $z_{\text{PQP}^+}^{(1)} \sim 3\text{ Å}$ and $z_{\text{PQP}^+}^{(2)} \sim 7\text{ Å}$, with relative weights of 72% and 21%, respectively. Such stratified bilayer configurations (as depicted in panel (a) of Fig. 4) are in competition with structures similar to ones shown in panel (d) of Fig. 4. Note that in parallel a far more complex height distribution of the perchlorate molecules sets in as soon as the now moderate electrostatic field allows them to proceed towards the interior of the slab: now, more than half of the ClO_4^- anions are located “in between” the PQP⁺ “layers”, trying on one side to compensate the charges of one or several PQP⁺ “partners” in the slab region and “filling spatial holes” wherever they can, on the other side. A large portion of perchlorate ions is even allowed to adsorb on the surface at a distance of $z_{\text{ClO}_4^-}^{(1)} \sim 4.074\text{ Å}$; note that these COM positions above the interface are larger than the minimal height of the PQP⁺ cations due to two reasons: if one face of the oxygen tetrahedron is oriented towards the interface (i.e., parallel to the gold surface), the COM of the ClO_4^- ion is increased by a value of $z_{\text{Cl}} - z_{\text{O}} \approx 0.492\text{ Å}$ with respect to the oxygen atoms. These atoms themselves have an equilibrium distance to the surface of $z_{\text{O}}^{(\text{eq})} \approx 3.582$ (evaluated

by minimizing Eq. (9) for a single oxygen atom with $\sigma_{\text{wO}}^{(\text{Mie})} = 3.630$, cf. Table 2), summing up to the presented minimal COM distance of the adsorbed ClO_4^- molecules from the interface. Note that the height distribution of the ClO_4^- ions is now rather broad (see Fig. 6), which is definitely owed to their relatively smaller size and their considerably higher mobility, as compared to their cationic counterparts (see also discussion below); these features make a conclusive interpretation of the roles of the ClO_4^- ions in the structure formation of the entire system rather difficult. Our interpretation is that the perchlorate ions are – due to their small spatial extent and their high mobility – able to compensate for local charge mismatches and to act as spatial spacers between the cations.

Decreasing further the magnitude of the electrostatic field down to $E_z \sim -0.1$ V/nm and $E_z \sim -0.01$ V/nm provides unambiguous evidence that the formation of the PQP^+ ions into bilayer structures become energetically more and more unfavourable, as the upper peak in the height distribution of the cations vanishes gradually. Concomitantly, an increasing number of perchlorate molecules approach the gold surface and are predominantly located there; possibly they act as a space filler on the surface itself while at the same time the small values of the electrostatic field keep the PQP^+ molecules near to the surface. In this context it should be noted that decreasing the electrostatic field is equivalent to decreasing the surface potential; thus and in combination with the adsorbed perchlorate molecules a transition from an auto-host-guest to a porous structure is plausible.

Eventually, at zero electric field the system exclusively gains energy from intramolecular interactions and adsorption on the gold surface. Since the perchlorate molecules are rather spherical in their shape they can efficiently adsorb onto the gold surface (in an orientation explained above), while the PQP^+ molecules are able to efficiently stack, especially without a guiding electrostatic field.

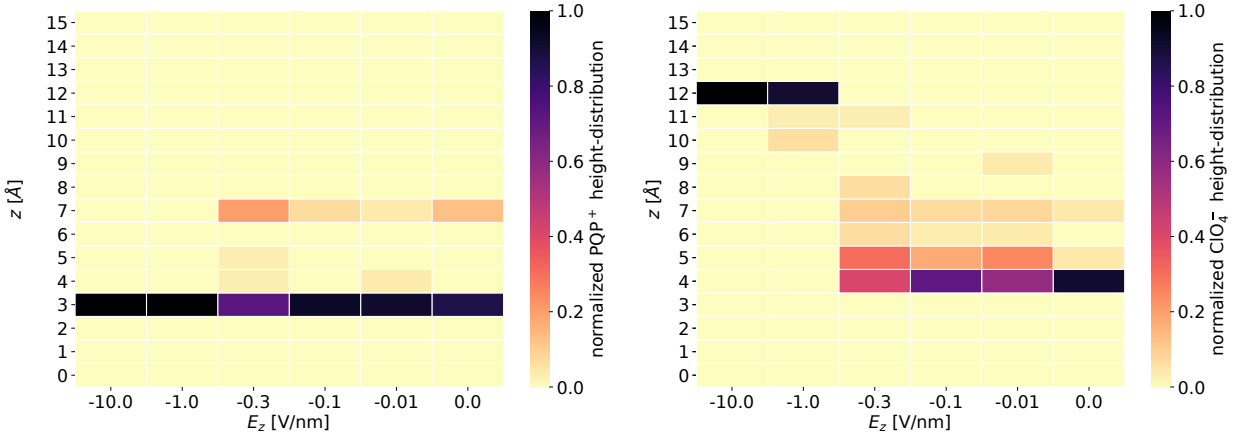


Figure 5: (color online) Height-distribution of PQP^+ (left) and ClO_4^- (right) molecules as functions of the considered values of the electrostatic field, E_z , normalized to the number of respective molecules (see colour code at the right hand side of the panels; the value of one means, that all respective molecules in all considered configurations are counted in one specific bin), see text for the energy considered in this analysis). Along the vertical axes the binning is performed in steps of one Å: $z = 0\text{Å}$ marks the position of the gold surface, the slab width amounts to 12Å .

4.2.3 The role of the perchlorate anions

We come back to the above mentioned volatility of the perchlorate ions: in Fig. 6 we present results from yet another evolutionary analysis: we now fix the positions and orientations of PQP^+ molecules as well as the extent and the shape of the unit-cell of some optimized configuration (as, for instance, depicted in panel (a) of Fig. 4) and vary only the degrees of freedom of the perchlorate anions. Fig. 6 shows – for fixed cell geometry and fixed PQP^+ positions and orientations – four structurally different perchlorate arrangements whose energy ranges within an interval of 38 meV (per $\text{PQP}^+-\text{ClO}_4^-$ pair): the fact that we obtain completely different configurations of the perchlorates (with essentially comparable energies) undoubtedly indicates the high mobility of the ClO_4^- ions. Changes in the structure, as one proceeds from left to right, are highlighted by respective circles (specifying the position of the “moving” perchlorate ion) and related arrows. The ClO_4^- molecules exhibit a remarkable freedom in their rotation without (or only marginally) changing the energy of a configuration;

this fact has rendered the minimization of the energy very difficult. However, it should also be noted that even translations can be performed without a substantial change in energy.

We note that the analysis of these different structures was achieved by using a so-called t-SNE⁹⁷ analysis on the leading five PCA components⁹⁸ of order parameters of all configurations identified by the evolutionary algorithm; for more detailed information on this rather technical issue we refer to Fig. 5 in subsection 4.2 of the Supplementary Information.

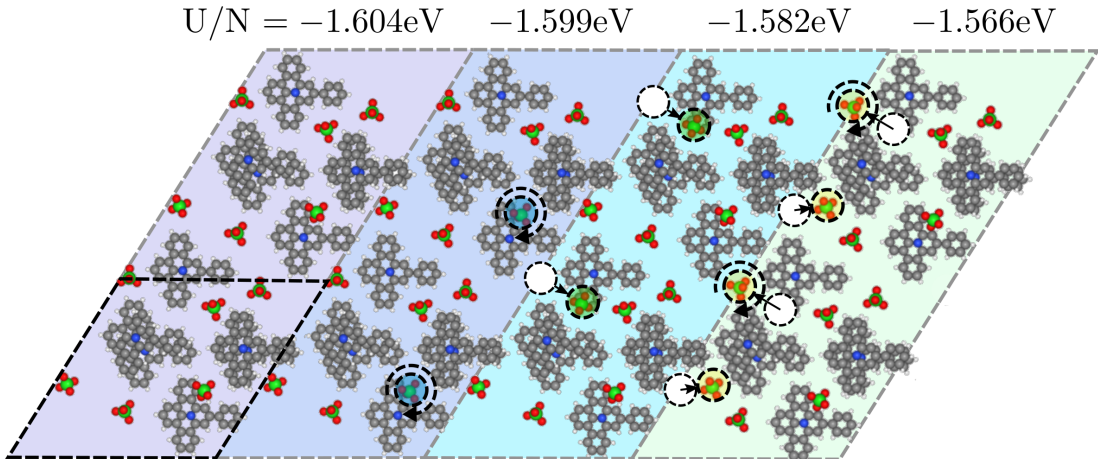


Figure 6: (color online) Four structurally different configurations of perchlorate ions (framed by gray, dashed lines and differently shaded areas) at optimized, fixed cell geometry (indicated in the bottom left corner by the black, dashed line) and optimized, fixed positions and orientations of the PQP^+ ions; the energies of these four configurations range within an interval of 38 meV (per $\text{PQP}^+-\text{ClO}_4^-$ pair), as obtained after an evolutionary energy minimization of solely the degrees of freedom of the ClO_4^- ions, starting from the configuration depicted in panel (a) of Fig. 4. Changes in the structure as one proceeds from left to right are highlighted by respective circles (specifying the position of the “moving” perchlorate ion) and arrows.

5 Conclusion and outlook

The prediction of supramolecular ordering of complex molecules at a metal–electrolyte interface using DFT based *ab initio* calculations is in view of the expected gigantic computational costs, and despite the availability of peta-scale computers, still an elusive enterprise. In this contribution we have proposed a two-stage alternative approach: (i) DFT-based *ab initio*

simulations provide reference data for the energies introduced in a classical model for the molecules involved, where each of their atomic entities are represented by a classical, spherical particle (with respective size, energy parameters, and charges). We modelled the interaction between the atomic entities and the metallic surface by a classical, perfectly conductive, Lennard-Jones like wall potential; the electrolyte is treated as a homogeneous, dielectric medium.

The inter-particle and particle-wall parameters were obtained via the following procedure: considering archetypical configurations (involving pairs of ions and/or ions located close to the surface) DFT energies were fitted by the related energy values of the classical model. (ii) The second step identifies the ordered ground state configurations of the molecules by minimizing the total energy of the now classical system. This optimization is based on evolutionary algorithms, which are known to operate efficiently and reliably even in high dimensional search spaces and for rugged energy surfaces.

Our new two-stage strategy overcomes the hitherto prohibitive computational cost of modelling the full system, while reproducing the key observations of a well-documented experimental system consisting of disc-shaped PQP^+ cations and ClO_4^- anions: as a function of increasing electric field at the metal–electrolyte interface, the molecular building blocks are seen to self-organize into an open porous structure, a self-host–guest pattern and a stratified bilayer. Future work will focus on verifying the extent of predictive power of our method towards molecular self-assembly under electrochemical conditions, and on strategies to further streamline and reduce the computational cost of our approach, without sacrificing the reliability of the predicted results.

In view of the high computational costs and the conceptual challenges encountered in our investigations we have pondered the question if the complexity of the current model (which – as a classical model – is comprehensive in the sense that it contains all atomistic features) could possibly be further reduced, avoiding thereby conceptual and computational bottlenecks. The idea behind this strategy is to develop – starting from the present model –

a hierarchy of ever simpler models where, for instance, larger sub-units of the molecule (such as aromatic rings) are replaced by disk shaped units carrying higher electrostatic moments, as schematically visualized in Fig. 7. Such a model might provide a first, semi-quantitative prediction of the self-assembly of the PQP^+ and of the ClO_4^- ions at considerably reduced costs and might help to pre-screen possibly promising portions of the huge parameter space for subsequent investigations of the full model. Efforts in this direction are currently pursued.

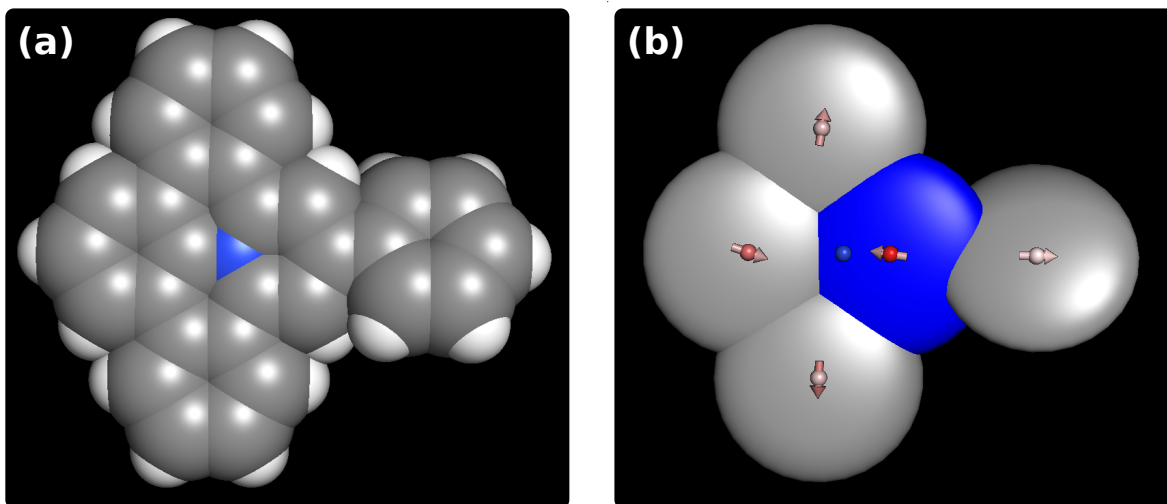


Figure 7: Panel (a): atomistic model of the PQP^+ molecule as used in this contribution (white: hydrogen atoms, grey: carbon atoms, and blue: nitrogen atom), see also Fig. 3 in the S.I.; panel (b): related coarse-grained model in a hierarchy of ever simpler models, using, e.g., Gay-Berne potentials to account for the van der Waals interaction of all atoms in the specific rings and a multi-pole expansion to second order (monopole as coloured points, dipole moments as small arrows) for the electrostatic interaction.

6 Acknowledgment

BH acknowledges a DOC Fellowship of the Austrian Academy of Sciences; further he gratefully acknowledges helpful discussions with Moritz Antlanger (Wien), Benjamin Rotenberg (Paris), and Martial Mazars (Paris-Sud) on several issues of this project and thanks the Freiburg Centre for Interactive Materials and Bioinspired Technologies (Universität Freiburg)

for the kind hospitality, where part of the work has been carried out. BH also acknowledges the Christiana Hörbiger prize for covering travel expenses to Paris. BH and GK acknowledge financial support by E-CAM, an e-infrastructure center of excellence for software, training and consultancy in simulation and modelling funded by the EU (Proj. No. 676531). The computational results presented have been achieved [in part] using the Vienna Scientific Cluster (VSC). SS and MW acknowledge funding from Deutsche Forschungsgemeinschaft (WA 1687/10-1) and the computing time granted by the John von Neumann Institute for Computing (NIC) within project HFR08 as well as the computational resource bwUni-Cluster funded by the Ministry of Science, Research and the Arts Baden-Württemberg and the Universities of the State of Baden-Württemberg, Germany, within the framework program bwHPC. MW is thankful for enlightening discussion with Johannes Fiedler and Stefan Buhmann. SFLM and GK gratefully acknowledge financial support within the TU Wien funded Doctoral College BIOINTERFACE. SFLM further acknowledges support from the Austrian Science Fund (FWF, “Boron Nitride Nanomesh for Actuated Self-Assembly” (I3256-N36)) and Energy Lancaster.

Table 1: Numerical results for the optimized LJ and Mie parameters, $\mathcal{M}^{(LJ)} = \{\sigma_i, \epsilon_i\}$ and $\mathcal{M}^{(Mie)} = \{\sigma_i, \epsilon_i, \gamma_i^{(R)}, \gamma_i^{(A)}\}$, for each element i , for the results depicted in the Fig. 3 (σ_i in Å and ϵ_i in meV). Reference values from the literature are listed in Table 1 in the supplementary information.

	σ_H	σ_C	σ_N	σ_O	σ_{Cl}	ϵ_H	ϵ_C	ϵ_N	ϵ_O	ϵ_{Cl}
$\mathcal{M}^{(LJ)}$	2.243	3.658	3.743	2.865	5.953	3.052	1.204	3.311	7.396	0.172
$\mathcal{M}^{(Mie)}$	2.236	3.703	3.328	2.428	4.956	3.999	0.946	2.021	11.481	5.289
	$\gamma_H^{(R)}$	$\gamma_C^{(R)}$	$\gamma_N^{(R)}$	$\gamma_O^{(R)}$	$\gamma_{Cl}^{(R)}$	$\gamma_H^{(A)}$	$\gamma_C^{(A)}$	$\gamma_N^{(A)}$	$\gamma_O^{(A)}$	$\gamma_{Cl}^{(A)}$
$\mathcal{M}^{(LJ)}$	12	12	12	12	12	6	6	6	6	6
$\mathcal{M}^{(Mie)}$	6.263	7.136	8.659	8.743	15.455	7.500	12.299	13.854	17.193	4.684

References

- (1) Cui, K.; Dorner, I.; Mertens, S. F. L. Interfacial supramolecular electrochemistry. *Current Opinion in Electrochemistry* **2018**, *8*, 156–163.

Table 2: Top row: Numerical results for LJ-length and well-depth parameters, σ_{wi} in Å and ϵ_{wi} in meV, between the wall and each element $i = [\text{H}, \text{C}, \text{N}]$ and $j = [\text{O}, \text{Cl}]$, grouped by the molecules they belong to (PQP⁺ and ClO₄⁻), for intermolecular short-range LJ parameters listed in Table. 1. Bottom row: corresponding σ_{wi} and ϵ_{wi} parameters for intermolecular short-range Mie-parameters also listed in Table. 1.

	$\sigma_{w[\text{H,C,N}]}$	$\sigma_{w[\text{O,Cl}]}$	$\epsilon_{w[\text{H,C,N}]}$	$\epsilon_{w[\text{O,Cl}]}$
$\mathcal{W}^{(\text{LJ})}$	3.197	3.625	3.741	15.781
$\mathcal{W}^{(\text{Mie})}$	3.208	3.630	3.698	20.167

Table 3: Results of evolutionary ground-state search for different electric field strengths, E_z , for different unit-cell areas, A and number of PQP⁺ molecules, N_{PQP} , each line represents a evolutionary search. The respective structures are presented in Fig. 4.

	E_z [Vnm ⁻¹]	U/N_{PQP} [eV]	N_{PQP}	A [nm ²]	N_{PQP}/A [nm ⁻²]
(a)	-0.30	-1.5804	6	8.5	0.705882
(b)	-0.10	-1.7276	6	11.75	0.510638
(d)	-0.10	-1.7274	5	8.0	0.625000
(c)	-0.01	-1.6445	6	11.25	0.533333
(f)	-0.01	-1.6364	6	12.25	0.489796
(e)	-0.01	-1.6332	7	11.75	0.595745

- (2) Mertens, S. F. L. In *Encyclopedia of Interfacial Chemistry: Surface Science and Electrochemistry*, 1st ed.; Wandelt, K., Ed.; Elsevier, 2018; Vol. 4; pp 13–23.
- (3) Cui, K.; Mali, K. S.; Ivasenko, O.; Wu, D.; Feng, X.; Walter, M.; Müllen, K.; De Feyter, S.; Mertens, S. F. L. Squeezing, then stacking: From breathing pores to three-dimensional ionic self-assembly under electrochemical control. *Angew. Chem Int. Edit.* **2014**, *53*, 12951–12954.
- (4) Cui, K.; Ivasenko, O.; Mali, K. S.; Wu, D.; Feng, X.; Müllen, K.; De Feyter, S.; Mertens, S. F. L. Potential-driven molecular tiling of a charged polycyclic aromatic compound. *Chem. Commun.* **2014**, *50*, 10376–10378.
- (5) Cui, K.; Mali, K. S.; Wu, D.; Feng, X.; Müllen, K.; Walter, M.; De Feyter, S.; Mertens, S. F. L. Reversible Anion-Driven Switching of an Organic 2D Crystal at a Solid–Liquid Interface. *Small* **2017**, *13*, 1–8.
- (6) Stillinger, F. H. Exponential multiplicity of inherent structures. *Phys. Rev. E* **1999**, *59*, 48–51.
- (7) Scherbela, M.; Hörmann, L.; Jeindl, A.; Obersteiner, V.; Hofmann, O. T. Charting the energy landscape of metal/organic interfaces via machine learning. *Phys. Rev. Materials* **2018**, *2*, 043803.
- (8) Blank, T. B.; Brown, S. D.; Calhoun, A. W.; Doren, D. J. Neural network models of potential energy surfaces. *J. Chem. Phys.* **1995**, *103*, 4129–4137.
- (9) Lorenz, S.; Groß, A.; Scheffler, M. Representing high-dimensional potential-energy surfaces for reactions at surfaces by neural networks. *Chem. Phys. Lett.* **2004**, *395*, 210–215.
- (10) Behler, J.; Parrinello, M. Generalized neural-network representation of high-dimensional potential-energy surfaces. *PRL* **2007**, *98*, 1–4.

- (11) Behler, J.; Lorenz, S.; Reuter, K. Representing molecule-surface interactions with symmetry-adapted neural networks. *J. Chem. Phys.* **2007**, *127*, 014705.
- (12) Behler, J. Perspective: Machine learning potentials for atomistic simulations. *J. Chem. Phys.* **2016**, *145*.
- (13) Schütt, K. T.; Kindermans, P. J.; Sauceda, H. E.; Chmiela, S.; Tkatchenko, A.; Müller, K. R. SchNet: A continuous-filter convolutional neural network for modeling quantum interactions. *Advances in Neural Information Processing Systems* **2017**, *2017-Decem*, 992–1002.
- (14) Unke, O. T.; Meuwly, M. PhysNet: A Neural Network for Predicting Energies, Forces, Dipole Moments, and Partial Charges. *J. Chem. Theory Comput.* **2019**, *15*, 3678–3693.
- (15) Cristianini, N.; Shawe-Taylor, J. *An Introduction to Support Vector Machines and Other Kernel-based Learning Methods*; Cambridge University Press, 2000.
- (16) Bartók, A. P.; Payne, M. C.; Kondor, R.; Csányi, G. Gaussian Approximation Potentials: The Accuracy of Quantum Mechanics, without the Electrons. *Phys. Rev. Lett.* **2010**, *104*, 136403.
- (17) Rupp, M.; Tkatchenko, A.; Müller, K.-R.; von Lilienfeld, O. A. Fast and Accurate Modeling of Molecular Atomization Energies with Machine Learning. *Phys. Rev. Lett.* **2012**, *108*, 058301.
- (18) Bartók, A. P.; Kondor, R.; Csányi, G. On representing chemical environments. *Phys. Rev. B* **2013**, *87*, 184115.
- (19) De, S.; Bartók, A. P.; Csányi, G.; Ceriotti, M. Comparing molecules and solids across structural and alchemical space. *Phys. Chem. Chem. Phys.* **2016**, *18*, 13754–13769.
- (20) De, S.; Bartók, A. P.; Csányi, G.; Ceriotti, M. Comparing molecules and solids across structural and alchemical space. *Phys. Chem. Chem. Phys.* **2016**, *18*, 13754–13769.

- (21) Obersteiner, V.; Scherbela, M.; Hörmann, L.; Wegner, D.; Hofmann, O. T. Structure Prediction for Surface-Induced Phases of Organic Monolayers: Overcoming the Combinatorial Bottleneck. *Nano Letters* **2017**, *17*, 4453–4460, PMID: 28640634.
- (22) Hörmann, L.; Jeindl, A.; Egger, A. T.; Scherbela, M.; Hofmann, O. T. SAMPLE: Surface structure search enabled by coarse graining and statistical learning. *Comput. Phys. Commun.* **2019**, *244*, 143 – 155.
- (23) Kaatze, U. Complex permittivity of water as a function of frequency and temperature. *J. Chem. Eng. Data* **1989**, *34*, 371–374.
- (24) Hamelin, J.; Mehl, J. B.; Moldover, M. R. The Static Dielectric Constant of Liquid Water Between 274 and 418 K Near the Saturated Vapor Pressure. *Int. J. Thermophys.* **1998**, *19*, 1359–1380.
- (25) Vargaftik, N. B.; Volkov, B. N.; Voljak, L. D. International Tables of the Surface Tension of Water. *J. Phys. Chem. Ref. Data* **1983**, *12*, 817–820.
- (26) Hasted, J. B.; Ritson, D. M.; Collie, C. H. Dielectric Properties of Aqueous Ionic Solutions. Parts I and II. *J. Chem. Phys.* **1948**, *16*, 1–21.
- (27) Gavish, N.; Promislow, K. Dependence of the dielectric constant of electrolyte solutions on ionic concentration: A microfield approach. *Phys. Rev. E* **2016**, *94*, 012611.
- (28) Mollerup, J. M.; Breil, M. P. Modeling the permittivity of electrolyte solutions. *AIChE Journal* **2015**, *61*, 2854–2860.
- (29) Fumagalli, L.; Esfandiar, A.; Fabregas, R.; Hu, S.; Ares, P.; Janardanan, A.; Yang, Q.; Radha, B.; Taniguchi, T.; Watanabe, K.; Gomila, G.; Novoselov, K. S.; Geim, A. K. Anomalously low dielectric constant of confined water. *Science* **2018**, *360*, 1339–1342.
- (30) Mortensen, J. J.; Hansen, L. B.; Jacobsen, K. W. Real-space grid implementation of the projector augmented wave method. *Phys. Rev. B* **2005**, *71*, 035109.

- (31) Enkovaara, J.; Rostgaard, C.; Mortensen, J. J.; Chen, J.; Duřak, M.; Ferrighi, L.; Gavnholt, J.; Glinśvad, C.; Haikola, V.; Hansen, H. A.; Kristoffersen, H. H.; Kuisma, M.; Larsen, A. H.; Lehtovaara, L.; Ljungberg, M.; Lopez-Acevedo, O.; Moses, P. G.; Ojanen, J.; Olsen, T.; Petzold, V.; Romero, N. A.; Stausholm-Møller, J.; Strange, M.; Tritsarīs, G. A.; Vanin, M.; Walter, M.; Hammer, B.; Håkkinen, H.; Madsen, G. K. H.; Nieminen, R. M.; Nørskov, J. K.; Puska, M.; Rantala, T. T.; Schiøtz, J.; Thygesen, K. S.; Jacobsen, K. W. Electronic structure calculations with GPAW: a real-space implementation of the projector augmented-wave method. *J. Phys. Condens. Matter* **2010**, *22*, 253202.
- (32) Larsen, A. H.; Mortensen, J. J.; Blomqvist, J.; Castelli, I. E.; Christensen, R.; Marcin Duřak; Friis, J.; Groves, M. N.; Hammer, B.; Hargus, C.; Hermes, E. D.; Jennings, P. C.; Jensen, P. B.; Kermode, J.; Kitchin, J. R.; Kolsbjerg, E. L.; Kubal, J.; Kristen Kaasbjerg; Lysgaard, S.; Maronsson, J. B.; Maxson, T.; Olsen, T.; Pastewka, L.; Andrew Peterson; Rostgaard, C.; Schiøtz, J.; Schütt, O.; Strange, M.; Thygesen, K. S.; Tejs Vegge; Vilhelmsen, L.; Walter, M.; Zeng, Z.; Jacobsen, K. W. The atomic simulation environmenta Python library for working with atoms. *J. Phys. Condens. Matter* **2017**, *29*, 273002.
- (33) Blöchl, P. E. Projector augmented-wave method. *Phys. Rev. B* **1994**, *50*, 17953–17979.
- (34) Perdew, J. P.; Burke, K.; Ernzerhof, M. Generalized gradient approximation made simple. *Phys. Rev. Lett.* **1996**, *77*, 3865–3868.
- (35) Tkatchenko, A.; Scheffler, M. Accurate Molecular Van Der Waals Interactions from Ground-State Electron Density and Free-Atom Reference Data. *Phys. Rev. Lett.* **2009**, *102*, 073005.
- (36) Held, A.; Walter, M. Simplified continuum solvent model with a smooth cavity based on volumetric data. *J. Chem. Phys.* **2014**, *141*, 174108.

- (37) Monkhorst, H. J.; Pack, J. D. Special points for Brillouin-zone integrations. *Phys. Rev. B* **1976**, *13*, 5188–5192.
- (38) Eisenschitz, R.; London, F. Über das Verhältnis der van der Waalsschen Kräfte zu den homöopolaren Bindungskräften. *Z. Phys.* **1930**, *60*, 491–527.
- (39) Fiedler, J.; Thiyam, P.; Kurumbail, A.; Burger, F. A.; Walter, M.; Persson, C.; Brevik, I.; Parsons, D. F.; Boström, M.; Buhmann, S. Y. Effective Polarizability Models. *J. Phys. Chem. A* **2017**, *121*, 9742–9751.
- (40) Beneduci, A. Which is the effective time scale of the fast Debye relaxation process in water? *J. Mol. Liq.* **2008**, *138*, 55–60.
- (41) Bukowski, R.; Szalewicz, K. Complete ab initio three-body nonadditive potential in Monte Carlo simulations of vaporliquid equilibria and pure phases of argon. *114*, 9518–9531, Publisher: American Institute of Physics.
- (42) McDaniel, J. G.; Schmidt, J. R. First-Principles Many-Body Force Fields from the Gas Phase to Liquid: A Universal Approach. *118*, 8042–8053, Publisher: American Chemical Society.
- (43) Tkatchenko, A.; DiStasio, R. A.; Car, R.; Scheffler, M. Accurate and Efficient Method for Many-Body van der Waals Interactions. *108*, 236402.
- (44) Perdew, J. P. Energetics of charged metallic particles: From atom to bulk solid. *Phys. Rev. B* **1988**, *37*, 6175–6180.
- (45) Serena, P. A.; Soler, J. M.; García, N. Self-consistent image potential in a metal surface. *Phys. Rev. B* **1986**, *34*, 6767–6769.
- (46) Lang, N. D.; Kohn, W. Theory of Metal Surfaces: Induced Surface Charge and Image Potential. *Phys. Rev. B* **1973**, *7*, 3541–3550.

- (47) Finnis, M. W.; Kaschner, R.; Kruse, C.; Furthmüller, J.; Scheffler, M. The interaction of a point charge with a metal surface: theory and calculations for (111), (100) and (110) aluminium surfaces. *J. Phys. Condens. Matter* **1995**, *7*, 2001.
- (48) Held, A.; Moseler, M.; Walter, M. Charging properties of gold clusters in different environments. *Phys. Rev. B* **2013**, *87*, 045411.
- (49) Chakrabarti, D.; Kusumaatmaja, H.; Rühle, V.; Wales, D. J. Exploring energy landscapes: From molecular to mesoscopic systems. *Phys. Chem. Chem. Phys.* **2014**, *16*, 5014–5025.
- (50) Chakrabarti, D.; Wales, D. J. Simulations of rigid bodies in an angle-axis framework. *Appl. Environ. Microbiol.* **2008**, *11*, 1970–1976.
- (51) Hansen, J.-P.; McDonald, I. R. *Theory of Simple Liquids: with Applications to Soft Matter*; Academic Press, 2013.
- (52) Mie, G. Zur kinetischen Theorie der einatomigen Körper. *Ann. Phys.* **1903**, *316*, 657–697.
- (53) Magda, J. J.; Tirrell, M.; Davis, H. T. Molecular dynamics of narrow, liquid-filled pores. *J. Chem. Phys.* **1985**, *83*, 1888–1901.
- (54) Jacob, T.; Sabo, L. *Reference Module in Chemistry, Molecular Sciences and Chemical Engineering*; 2015.
- (55) Plimpton, S. Fast Parallel Algorithms for Short – Range Molecular Dynamics. *J. Comput. Phys.* **1995**, *117*, 1–19.
- (56) Mazars, M. Long ranged interactions in computer simulations and for quasi-2D systems. *Phys. Rep.* **2011**, *500*, 43–116.
- (57) Smith, E. R. Electrostatic Energy in Ionic Crystals. *Proc. Royal Soc. Lond.* **1981**, *375*, 475–505.

- (58) Yeh, I. C.; Berkowitz, M. L. Ewald summation for systems with slab geometry. *J. Chem. Phys.* **1999**, *111*, 3155.
- (59) Bader, R. F. W. Atoms in Molecules. *Acc. Chem. Res.* **1985**, *18*, 9–15.
- (60) Hartl, B.; Sharma, S.; Walter, M.; Mertens, S. F. L.; Kahl, G. Phase behaviour of supramolecular ordering of complex molecules under electrochemical conditions. **to be published**,
- (61) Gottwald, D.; Kahl, G.; Likos, C. N. Predicting equilibrium structures in freezing processes Predicting equilibrium structures in freezing processes. *J. Chem. Phys.* **2005**, *122*, 204503.
- (62) Fornleitner, J.; Lo Verso, F.; Kahl, G.; Likos, C. N. Genetic algorithms predict formation of exotic ordered configurations for two-component dipolar monolayers . *Soft Matter* **2008**, *4*, 480–484.
- (63) Fornleitner, J.; Lo Verso, F.; Kahl, G.; Likos, C. N. Ordering in Two-Dimensional Dipolar Mixtures. *Langmuir* **2009**, *25*, 7836–7846.
- (64) Doppelbauer, G.; Bianchi, E.; Kahl, G. Self-assembly scenarios of patchy colloidal particles in two dimensions. *J. Phys. Condens. Matter* **2010**, *22*, 104105.
- (65) Fornleitner, J.; Kahl, G. Pattern formation in two-dimensional square-shoulder systems. *J. Phys. Condens. Matter* **2010**, *22*, 104118.
- (66) "Doppelbauer, G.; Noya, E. G.; Bianchi, E.; Kahl, G. "Self-assembly scenarios of patchy colloidal particles". *Soft Matter* **2012**, *8*, 7768–7772.
- (67) Antlanger, M.; Kahl, G.; Mazars, M.; Šamaj, L.; Trizac, E. Rich Polymorphic Behavior of Wigner Bilayers. *Phys. Rev. Lett.* **2016**, *117*, 118002.
- (68) Virtanen, P.; Gommers, R.; Oliphant, T. E.; Haberland, M.; Reddy, T.; Cournapeau, D.; Burovski, E.; Peterson, P.; Weckesser, W.; Bright, J.; van der Walt, S. J.;

Brett, M.; Wilson, J.; Jarrod Millman, K.; Mayorov, N.; Nelson, A. R. J.; Jones, E.; Kern, R.; Larson, E.; Carey, C.; Polat, İ.; Feng, Y.; Moore, E. W.; Vand erPlas, J.; Laxalde, D.; Perktold, J.; Cimrman, R.; Henriksen, I.; Quintero, E. A.; Harris, C. R.; Archibald, A. M.; Ribeiro, A. H.; Pedregosa, F.; van Mulbregt, P.; Contributors, S. . . SciPy 1.0–Fundamental Algorithms for Scientific Computing in Python. 2019.

- (69) Kraft, D. *A software package for sequential quadratic programming*; 1988; pp DFVLR–FB 88–28.
- (70) Dalcín, L. D.; Paz, R. R.; Storti, M. MPI for Python. *J. Parallel Distr. Com.* **2005**, *65*, 1108–1115.
- (71) Dalcín, L. D.; Paz, R. R.; Storti, M.; Elía, J. D. MPI for Python : Performance improvements and MPI-2 extensions. *J. Parallel Distr. Com.* **2008**, *68*, 655–662.
- (72) Dalcín, L. D.; Paz, R. R.; Kler, P. A.; Cosimo, A. Parallel distributed computing using Python. *Adv. Water Resour.* **2011**, *34*, 1124–1139.
- (73) Mascato, P. *On Evolution, Search, Optimization, Genetic Algorithms and Martial Arts*; 1989; p 67.
- (74) Gottwald, D. Genetic Algorithms in Condensed Matter Theory. Ph.D. thesis, TU Wien, 2005.
- (75) Doppelbauer, G. Ordered Equilibrium Structures of Patchy Particle Systems. Ph.D. thesis, TU Wien, 2012.
- (76) Fornleitner, J.; Kahl, G. Lane formation vs . cluster formation in two- dimensional square-shoulder systems A genetic algorithm approach Lane formation vs . cluster formation in two-dimensional square-shoulder systems A genetic algorithm approach. *EPL* **2008**, *82*, 18001.

- (77) Antlanger, M. Ordered equilibrium structures in systems with long-range interactions. Ph.D. thesis, TU Wien, 2015.
- (78) Darwin, C. *On the origin of species by means of natural selection, or preservation of favoured races in the struggle for life*; London : John Murray, 1859.
- (79) Hartke, B. Global geometry optimization of clusters using genetic algorithms. *J. Phys. Chem.* **1993**, *97*, 9973–9976.
- (80) Hartke, B. Global cluster geometry optimization by a phenotype algorithm with Niches: Location of elusive minima, and low-order scaling with cluster size. *J. Comput. Chem.* **1999**, *16*, 1752–1759.
- (81) Pannetier, J.; Bassas-Alsina, J.; Rodriguez-Carvajal, J.; Caignaert, V. Prediction of crystal structures from crystal chemistry rules by simulated annealing. *Nature* **1990**, *346*, 343–345.
- (82) Schön, J. C.; Jansen, M. In *Modern Methods of Crystal Structure Prediction*; Oganov, A. R., Ed.; WILEY-VCH Verlag GmbH & Co. KGaA, 2015; pp 67–105.
- (83) Wales, D. J.; Doye, J. P. K. Global Optimization by Basin-Hopping and the Lowest Energy Structures of Lennard-Jones Clusters Containing up to 110 Atoms. *J. Phys. Chem. A* **1997**, *101*, 5111–5116.
- (84) Panosetti, C.; Krautgasser, K.; Palagin, D.; Reuter, K.; Maurer, R. J. Global Materials Structure Search with Chemically Motivated Coordinates. *Nano Letters* **2015**, *15*, 8044–8048, PMID: 26444084.
- (85) Krautgasser, K.; Panosetti, C.; Palagin, D.; Reuter, K.; Maurer, R. J. Global structure search for molecules on surfaces: Efficient sampling with curvilinear coordinates. *J. Chem. Phys.* **2016**, *145*, 084117.

- (86) Goedecker, S. Minima hopping: An efficient search method for the global minimum of the potential energy surface of complex molecular systems. *J. Chem. Phys.* **2004**, *120*, 9911–9917.
- (87) Goedecker, S. In *Modern Methods of Crystal Structure Prediction*; Oganov, A. R., Ed.; WILEY-VCH Verlag GmbH & Co. KGaA, 2015; pp 131–145.
- (88) Abraham, N. L.; Probert, M. I. J. A periodic genetic algorithm with real-space representation for crystal structure and polymorph prediction. *Phys. Rev. B* **2006**, *73*, 224104.
- (89) Deaven, D. M.; Ho, K. M. Molecular Geometry Optimization with a Genetic Algorithm. *Phys. Rev. Lett.* **1995**, *75*, 288–291.
- (90) Lyakhov, A. O.; Oganov, A. R.; Valle, M. In *Modern Methods of Crystal Structure Prediction*; Oganov, A. R., Ed.; WILEY-VCH Verlag GmbH & Co. KGaA, 2015; pp 147–180.
- (91) Supady, A.; Blum, V.; Baldauf, C. First-Principles Molecular Structure Search with a Genetic Algorithm. *J. Chem. Inf. Model.* **2015**, *55*, 2338–2348.
- (92) Senior, A. W.; Evans, R.; Jumper, J.; Kirkpatrick, J.; Sifre, L.; Green, T.; Qin, C.; Židek, A.; Nelson, A. W. R.; Bridgland, A.; Penedones, H.; Petersen, S.; Simonyan, K.; Crossan, S.; Kohli, P.; Jones, D. T.; Silver, D.; Kavukcuoglu, K.; Hassabis, D. Improved protein structure prediction using potentials from deep learning. *Nature* **2020**, *577*, 706–710.
- (93) Silver, D.; Schrittwieser, J.; Simonyan, K.; Antonoglou, I.; Huang, A.; Guez, A.; Hubert, T.; Baker, L.; Lai, M.; Bolton, A.; Chen, Y.; Lillicrap, T.; Hui, F.; Sifre, L.; van den Driessche, G.; Graepel, T.; Hassabis, D. Mastering the game of Go without human knowledge. *Nature* **2017**, *550*, 354–359.

- (94) Hanke, F. Sensitivity analysis and uncertainty calculation for dispersion corrected density functional theory. *J. Comput. Chem.* **2011**, *32*, 1424–1430.
- (95) Berland, K.; Cooper, V. R.; Lee, K.; Schröder, E.; Thonhauser, T.; Hyldgaard, P.; Lundqvist, B. I. van der Waals forces in density functional theory: a review of the vdW-DF method. *Rep. Prog. Phys.* **2015**, *78*, 066501.
- (96) Stöhr, M.; Voorhis, T. V.; Tkatchenko, A. Theory and practice of modeling van der Waals interactions in electronic-structure calculations. *Chem. Soc. Rev.* **2019**, *48*, 4118–4154.
- (97) Maaten, L. V. D.; Hinton, G. Visualizing Data using t-SNE. *J. Mach. Learn. Res* **2008**, *9*, 2579–2605.
- (98) Jolliffe, I. *Principal component analysis*; Springer Verlag: New York, 2002.

Supplementary information for Reliable computational prediction of supramolecular ordering of complex molecules under electrochemical conditions

Benedikt Hartl,[†] Shubham Sharma,[‡] Oliver Brügger,[‡] Stijn F. L. Mertens,^{¶,§}
Michael Walter,^{‡,||,⊥} and Gerhard Kahl[†]

[†]*Institute for Theoretical Physics and Center for Computational Materials Science (CMS),
TU Wien, Wien, Austria*

[‡]*FIT Freiburg Centre for Interactive Materials and Bioinspired Technologies,
Georges-Köhler-Allee 105, 79110 Freiburg, Germany*

[¶]*Department of Chemistry, Lancaster University, Lancaster LA1 4YB, United Kingdom*

[§]*Institute of Applied Physics, TU Wien, Wien, Austria*

^{||}*Cluster of Excellence livMatS @ FIT - Freiburg Center for Interactive Materials and
Bioinspired Technologies, University of Freiburg, Georges-Köhler-Allee 105, D-79110
Freiburg, Germany*

[⊥]*Fraunhofer IWM, MikroTribologie Centrum μ TC, Wöhlerstrasse 11, 79108 Freiburg,
Germany*

E-mail:

1 Introduction

In the Supplementary Information (S.I.) we have collected relevant information which might considerably deteriorate the readability of the main text if it were placed there; still, the details presented in this document might be of relevance for an interested reader of the main text. For simplicity we have used in this document exactly the same section headings as in the main text; this will hopefully help to establish the appropriate association between the respective text passages.

2 The system and its representations

2.1 Convergence of theoretical calculations

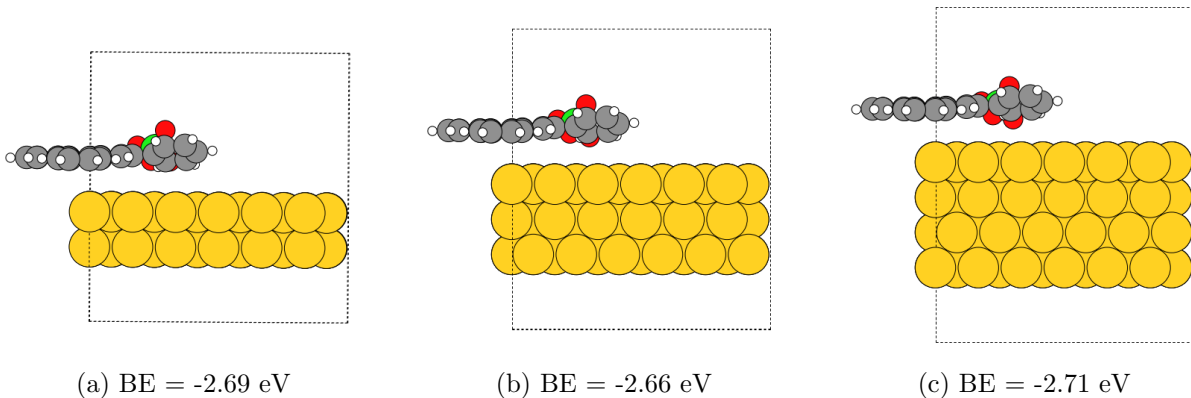


Figure 1: Schematic views of PQP^+ and ClO_4^- ions, located above gold surfaces built up by different numbers of layers. Below each panel the respective binding energies (BE) are specified.

The DFT-based binding energies of the PQP^+ and ClO_4^- ions were calculated for different numbers of gold layers with a constraint of fixed gold layers in an effort to study the convergence of the results with respect to the number of layers that build up the gold surface. The values for the binding energies, obtained for the different cases, are specified below the respective panels of Fig. 1; the panels themselves provide schematic plots for the different

types of gold layers. In the related DFT calculations we did not consider the van der Waals scaling, i.e., we chose $\omega_S \equiv 1$ in Eq. (1) of the main text.

We further examined the effect of fixing the gold atoms on the binding energy of PQP^+ and ClO_4^- ions to the surface. Allowing the uppermost gold layer to relax changed the binding energies to -2.73 eV, -2.69 eV and -2.73 eV for two, three and four layers, respectively. These values are well in accordance with the previously calculated values reported in Fig. 1. We therefore can conclude that fixing the gold atoms has a negligible effect on the binding energy obtained.

The calculated values for the binding energy obtained for two, three, and four layers of gold provide evidence that our choice for a two layer gold surface is sufficient to proceed with our calculation of the self-assembly scenarios of PQP^+ and ClO_4^- ions on this Au(111) surface. Local density of states were also plotted with respect to the energies of the corresponding states relative to the Fermi-level. The plotted density curves shows that the density of states for PQP^+ and ClO_4^- ions are quite similar irrespective of the number of layers of gold surface.

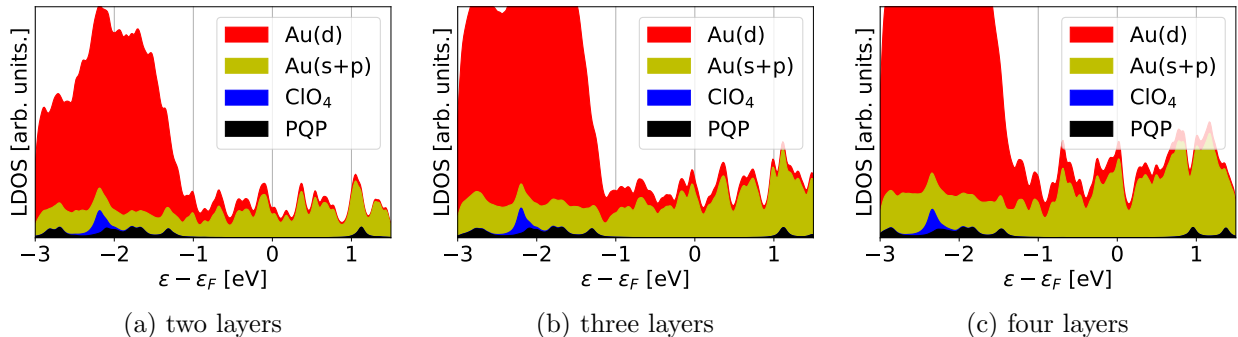


Figure 2: Local density of states (LDOS) relative to Fermi-level. The Kohn-Sham energies were projected on local atomic orbitals of Cl and O (ClO_4), C, N and H (PQP), and on gold s+p and d states, respectively.

Fig. 2 compares the density of Kohn-Sham states projected on the atomic species for the models depicted in Fig. 1. While the density of states of the gold part increases naturally with the number of gold layers, this has only marginal effects on the positions of the PQP^+

and ClO_4^- related states.

2.2 Angle-axis framework expressing rigid body orientations

In the optimization procedure put forward in Section 3 of the main text we rely on the angle-axis framework^{1,2} to express the orientation of rigid molecules within the lab-frame: closely related to the descriptions of rotations based on unit-quaternions,³⁻⁵ we introduce a three-component angle-axis vector, $\mathbf{P} = (P_1, P_2, P_3) = \theta \hat{\mathbf{P}}$, which defines an angle, $\theta = \sqrt{P_1^2 + P_2^2 + P_3^2}$, and a unit-vector, $\hat{\mathbf{P}}$, which represents the axis of the molecule; both are sufficient to describe any rotation of a rigid body in three dimensions. As discussed in Ref. 2 and following Rodrigues' rotation formula, the 3×3 rotation matrix $\mathbb{T}(\mathbf{P})$ associated with the angle-axis vector \mathbf{P} is given by

$$\mathbb{T}(\mathbf{P}) = \mathbb{I} + (1 - \cos \theta) \tilde{\mathbb{P}}\tilde{\mathbb{P}} + (\sin \theta) \tilde{\mathbb{P}}; \quad (1)$$

here \mathbb{I} is the 3×3 identity matrix and $\tilde{\mathbb{P}}$ is the skew-symmetric 3×3 matrix obtained from the components of the vector $\hat{\mathbf{P}}$ via

$$\tilde{\mathbb{P}} = \frac{1}{\theta} \begin{pmatrix} 0 & -P_3 & P_2 \\ P_3 & 0 & -P_1 \\ -P_2 & P_1 & 0 \end{pmatrix}. \quad (2)$$

In order to transform the coordinates of an atom, $\mathbf{r}_m^{(I)}$, defined in the center-of-mass system of molecule I to its lab-frame position, \mathbf{r}_m , the following transformation needs to be realized:

$$\mathbf{r}_m = \mathbf{R}_I + \mathbb{T}(\mathbf{P}_I) \cdot \mathbf{r}_m^{(I)}; \quad (3)$$

here \mathbf{R}_I is the center-of-mass coordinate of molecule I and $\mathbb{T}(\mathbf{P}_I)$ is the rotation matrix associated with the angle-axis vector \mathbf{P}_I of molecule I , as defined above.

2.3 Short-range potentials and parametrization

The short-range Mie potential, defined in Eq. (5) of the main text (Subsection 2.3.1), can be considered as a generalization of the Lennard-Jones (LJ) interaction:⁶ if the exponents of the repulsive and attractive parts of the potential are chosen as $\gamma_{ij}^{(R)} = 12$ and $\gamma_{ij}^{(A)} = 6$ the amplitude C_{ij} , given by Eq. (6) of the main text, becomes $C_{ij} = 4$ and the Mie-potential reduces to the well known LJ form.

During the fitting procedure put forward in Subsection 2.3.2 of the main text, it occurred at some instances that $\gamma_i^{(R)} < \gamma_i^{(A)}$. In such a case the defining equation for the C_{ij} (see Eq. (5) of the main text) guarantees that both the repulsive and the attractive parts of the potential maintain their respective features.

In Fig. 3 we depict the PQP^+ and the ClO_4^- ions using the actual values for the fitted Mie length parameters, σ_i (listed in Table 1 of the main text), as van der Waals radii. In Table 1 of the S.I. we list – for comparison – also the LJ length parameters for the atomic entities of the PQP^+ and the ClO_4^- molecules as they are commonly used in literature.

Table 1: LJ length parameters σ_i (in Å) for hydrogen (H), carbon (C), nitrogen (N), oxygen (O), and chlorine (Cl) from literature as defined in the *mendeleev*-python-module (*ver. 0.5.1*) and, as comparison, model parameters $\sigma_i^{(\text{LJ})}$ and $\sigma_i^{(\text{Mie})}$ from Table 1 in the main text.

	σ_{H}	σ_{C}	σ_{N}	σ_{O}	σ_{Cl}
mendeleev	2.2	3.4	3.1	3.04	3.5
alvarez	2.4	3.54	3.32	3.0	3.64
bondi	2.4	3.4	3.1	3.04	3.5
dreiding	3.195	3.8983	3.6621	3.4046	3.9503
mm3	3.24	4.08	3.86	3.64	4.14
uff	2.886	3.851	3.66	3.5	3.947
$\sigma_i^{(\text{LJ})}$	2.243	3.658	3.743	2.865	5.953
$\sigma_i^{(\text{Mie})}$	2.236	3.703	3.328	2.428	4.956

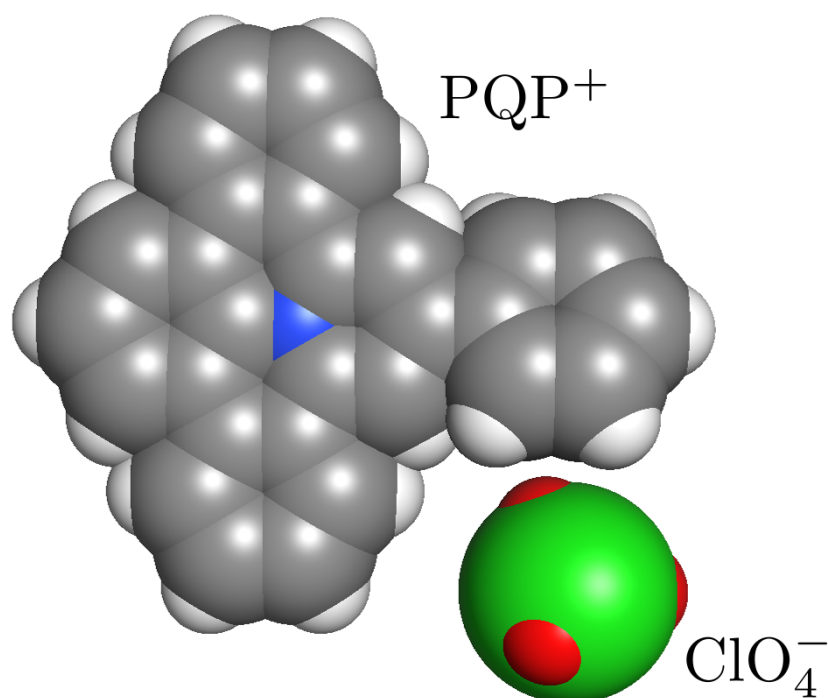


Figure 3: (Color online) Schematic representation of a PQP^+ and a ClO_4^- ion using the actual values of the fitted Mie length parameters $\sigma_i^{(\text{Mie})}$ for the short-range interactions introduced in Subsection 2.3.1 of the main text: atomic entities are shown as spheres with their diameters fixed by their respective optimized $\sigma_i^{(\text{Mie})}$ -values; these entities are colored according to the following scheme: hydrogen (white), carbon (gray), nitrogen (blue), chlorine (green), and oxygen (red).

In Tables 2 and 3 we list the coordinates of all atomic units and their associated partial charges (extracted via a Bader analysis^{7,8}) obtained from the relaxed DFT-structures of the PQP⁺ and ClO₄⁻ ions which serve as rigid molecular blueprints in the main text. Since the PQP⁺ cation is built up by 48 atomic units we have supplemented Table 2 by Fig. 4, indicating the labeling of the different atomic entities. In contrast, as the ClO₄⁻ molecule (see Table 3) is only built up by five atomic units, we have refrained in this case from a schematic presentation of the molecule.

Table 2: Atomic units building up the PQP⁺ ion, labeled by the index i according to the schematic view of the molecule presented in Fig. 4. The positions of these entities (x_i , y_i and z_i , and all in Å), as they were obtained in a relaxed DFT-based configuration, are given with respect to the center-of-mass of the molecule, marked in this figure by a cross. Furthermore, the respective charges of the atomic units, q_i (given in units of the elementary charge e), are obtained in a Bader analysis;⁷ these charges are directly transferred to our classical model of the PQP⁺ molecule.

i	element	x_i	y_i	z_i	q_i	i	element	x_i	y_i	z_i	q_i
1	C	0.1267	1.2051	-0.0253	0.3807	25	C	-4.8220	0.0601	-0.0341	-0.0565
2	N	-0.5941	0.0077	-0.0830	-1.1646	26	H	-4.7122	-2.0727	-0.0499	0.1101
3	C	-2.0123	0.0254	-0.0936	0.3949	27	C	-2.7268	-3.7034	-0.1427	-0.0931
4	C	0.0988	-1.2077	-0.0664	0.4209	28	H	1.1435	-3.7411	-0.1704	0.1265
5	C	-0.5685	2.4836	-0.0704	0.0642	29	C	-0.6337	-4.9026	-0.1737	-0.1096
6	C	1.5102	1.1636	0.0881	-0.0066	30	H	-3.7189	3.8240	-0.1608	0.0990
7	C	-2.7073	1.2652	-0.0766	0.0497	31	C	-1.9108	4.9519	-0.1507	-0.0561
8	C	-2.7389	-1.1964	-0.0946	0.0300	32	H	0.0658	5.8448	-0.1588	0.0863
9	C	-0.6299	-2.4673	-0.1204	-0.0401	33	C	4.4671	1.0567	-0.2093	-0.0996
10	C	1.4854	-1.2014	0.0175	-0.0272	34	C	4.3714	-1.1639	0.7541	-0.0342
11	C	-1.9791	2.5216	-0.0929	-0.0412	35	H	-5.9114	0.0745	-0.0008	0.1122
12	C	0.1514	3.7017	-0.0977	-0.0507	36	H	-3.8146	-3.7276	-0.1477	0.0984
13	H	2.0403	2.1040	0.1899	0.1396	37	C	-2.0369	-4.9037	-0.1638	0.0333
14	C	2.2322	-0.0280	0.1088	0.0058	38	H	-0.0809	-5.8419	-0.2001	0.1258
15	C	-4.1099	1.2499	-0.0437	-0.0944	39	H	-2.4371	5.9066	-0.1831	0.1140
16	C	-4.1411	-1.1474	-0.0630	-0.0382	40	H	3.9741	1.9279	-0.6429	0.0888
17	C	-2.0415	-2.4705	-0.1202	0.0066	41	C	5.8578	1.0346	-0.1202	-0.0392
18	C	0.0574	-3.7037	-0.1539	-0.0731	42	H	3.8020	-2.0184	1.1245	0.0943
19	H	1.9993	-2.1557	0.0110	0.1087	43	C	5.7627	-1.1824	0.8408	-0.1172
20	C	-2.6331	3.7708	-0.1343	-0.0780	44	H	-2.5876	-5.8452	-0.1777	0.1138
21	H	1.2385	3.7123	-0.0996	0.0676	45	H	6.4355	1.8929	-0.4673	0.1010
22	C	-0.5084	4.9176	-0.1347	0.0077	46	C	6.5117	-0.0860	0.4007	-0.0581
23	C	3.7024	-0.0450	0.2216	-0.0045	47	H	6.2672	-2.0562	1.2563	0.1042
24	H	-4.6584	2.1881	-0.0183	0.0912	48	H	7.6004	-0.1048	0.4614	0.1070

Table 4 compares the Bader charges of single PQP⁺ and ClO₄⁻ pairs in the gas phase and on the gold surface. This analysis reveals that the local charges on the ions are very similar

Table 3: Atomic units building up the ClO_4^- molecule. The positions of these entities (x_i , y_i and z_i , and all in Å), as they were obtained in a relaxed DFT-based configuration, are given with respect to the center-of-mass of the molecule, which coincides with the position of the oxygen atom. Furthermore, the respective charges of the atomic units, q_i (given in units of the elementary charge e), are obtained in a Bader analysis;⁷ these charges are directly transferred to our classical model of the ClO_4^- molecule.

i	element	x_i	y_i	z_i	q
1	Cl	0.0000	0.0000	0.0000	2.6996
2	O	1.4732	-0.0020	0.0000	-0.9249
3	O	-0.4916	1.3888	0.0000	-0.9249
4	O	-0.4917	-0.6933	1.2034	-0.9249
5	O	-0.4917	-0.6933	-1.2034	-0.9249

Table 4: Charges obtained in Bader analysis for PQP^+ , ClO_4^- ions in the gas phase and supported by the gold surface. The *on top* (OT) and *side by side* (SBS) configurations correspond to the configurations of single PQPClO_4 pairs as in Figs. 3 a) and b) of the main text, respectively. The SBS configuration on gold is depicted in Fig. 1a). The atom specific charges are summed values of all M atoms of the same type.

	on top (OT)	side by side (SBS)	SBS on gold support
PQP^+	1.0	0.9	0.9
N ($M = 1$)	-1.1	-1.1	-1.2
C ($M = 29$)	0.2	0.3	0.3
H ($M = 18$)	1.9	1.7	1.8
ClO_4^-	-1.0	-0.9	-1.0
Cl ($M = 1$)	2.6	2.5	2.7
O ($M = 4$)	-3.6	-3.5	-3.7
Au ($M = 72$)	—	—	0.1

in both environments and practically unaffected by the presence of the metal surface.

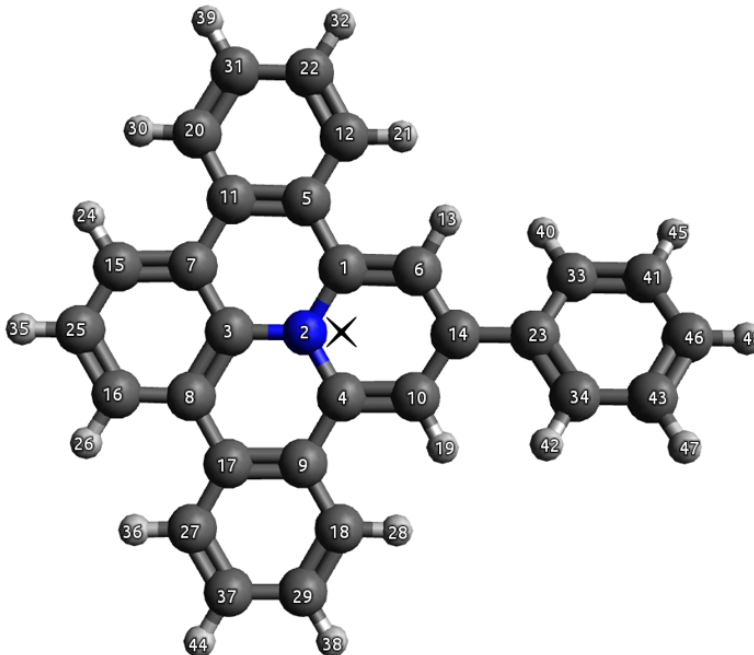


Figure 4: (Color online) Schematic view of the PQP^+ ion where its atomic constituents and the related bonds are depicted. The spheres are colored according to the respective chemical element: hydrogen (white), carbon (gray), and nitrogen (blue). The atomic constituents are labeled by indices $i = 1$ to $N_{\text{PQP}} = 48$; the positions of each of these entities (with respect to the center-of-mass of the molecule) are listed in Table 2. The black cross marks the center of mass, \mathbf{R}_{PQP} , of the PQP^+ molecule.

2.4 Image charges in a solvent

We may describe the electrostatic interaction between a charge distribution and a metallic surface by the method of image charges.⁹ The electric field inside a metal is completely screened and therefore the field on the surface can only be perpendicular to the metal surface.

Inside media the Maxwell equation for the displacement field $\mathbf{D}(\mathbf{r}, t)$ reads

$$\nabla \cdot \mathbf{D} = -4\pi\epsilon_0\rho \quad (4)$$

where ϵ_0 is the permittivity of the vacuum and $\rho(\mathbf{r}, t)$ a charge density. The relative permittivity ϵ_r of the medium connects to the electric field $\mathbf{E}(\mathbf{r}, t)$ to $\mathbf{D}(\mathbf{r}, t)$ via $\mathbf{D}(\mathbf{r}, t) = \epsilon_0\epsilon_r\mathbf{E}(\mathbf{r}, t)$. The Maxwell equation (4) then becomes

$$\nabla \cdot \epsilon_r\mathbf{E}(\mathbf{r}, t) = -4\pi\rho(\mathbf{r}, t). \quad (5)$$

A spatially constant permittivity ϵ_r thus leads to

$$\nabla \cdot \mathbf{E}(\mathbf{r}, t) = -4\pi\frac{\rho(\mathbf{r}, t)}{\epsilon_r} \quad (6)$$

which is the Maxwell equation in vacuum with a charge density scaled by the relative permittivity.

A slab geometry with a planar, perfectly conductive lower surface of infinite extend, separating the slab region from the interior bulk region at $z = 0$ can be modeled by image charges. These are placed within the bulk according to Eq. (7) in the main text, i.e. $\mathbf{r}_i = (x_i, y_i, z_i) \rightarrow (x_i, y_i, -z_i) = \mathbf{r}_{i'}$ and $q_{i'} \rightarrow -q_i$ and fulfill metallic boundary conditions. Including the constant electrostatic field E_z introduced in Eq. (10) in the main text this setting corresponds to the electrostatic potential $\Phi(\mathbf{r})$ of the form

$$\Phi(\mathbf{r}) = \frac{1}{4\pi\epsilon} \sum_{i=1}^n q_i \left(\frac{1}{|\mathbf{r} - \mathbf{r}_i|} - \frac{1}{|\mathbf{r} - \mathbf{r}_{i'}|} \right) + z E_z \Theta(z), \quad (7)$$

where $\Theta(z)$ is the Heaviside Theta (or step) function which is 0 if $z \leq 0$ and 1 otherwise. The potential vanishes at $z = 0$ in the entire x, y plane, i.e. $\Phi(\mathbf{r}_{xy} = (x, y, z = 0)) = 0$. In fact, every term in the sum vanishes separately as we have $|\mathbf{r}_{xy} - \mathbf{r}_i|^2 = (x - x_i)^2 + (y - y_i)^2 + (\pm z_i)^2 = |\mathbf{r}_{xy} - \mathbf{r}_{i'}|^2$, ensuring metallic boundary conditions.⁹

3 Identifications of self-assembly scenarios

3.1 Angle-axis gradient as calculated from the torque

The software package LAMMPS¹⁰ allows to evaluate forces and torques of rigid molecules enclosed in a simulation box. Since we are interested in the gradient of the potential energy with respect to angle-axis vectors, \mathbf{P} , i.e., $\nabla_{\mathbf{P}}U = (\frac{\partial U}{\partial P_1}, \frac{\partial U}{\partial P_2}, \frac{\partial U}{\partial P_3})$, we present here the transformation which is required to transform a three dimensional torque $\mathbf{T} = (T_x, T_y, T_z)$ to an angle-axis gradient, $\nabla_{\mathbf{P}}U$, or in a component-wise notation $\frac{\partial U}{\partial P_i} = \partial_i U$, using Latin indices $i = 1, 2, 3$ for three dimensional vectors.

In LAMMPS orientations are expressed in terms of unit-quaternions via the four dimensional vector $\mathbf{Q}^{(4)}$ (using Greek indices $\nu = 0, 1, 2, 3$)

$$\mathbf{Q}^{(4)} = (\cos \frac{\theta}{2}, \sin \frac{\theta}{2} \hat{\mathbf{P}}) = (Q_0, Q_1, Q_2, Q_3), \quad (8)$$

where, as described in Subsection 2.2 of the S.I., $\theta = |\mathbf{P}|$ is the angle of rotation around the axis $\hat{\mathbf{P}} = \mathbf{P}/\theta$ and $|\mathbf{Q}^{(4)}| = 1$.

Following the documentation of LAMMPS⁵ the resulting (four dimensional) torque vector, $\mathbf{T}^{(4)} = (0, T_x, T_y, T_z) = (0, \mathbf{T})$ on a rigid body is specified via

$$\mathbf{T}^{(4)} = -\frac{1}{2} \mathbb{S}_{4 \times 4}^T \nabla_{\mathbf{Q}^{(4)}} U + \mathbf{T}_{\text{int}}^{(4)}. \quad (9)$$

The internal torque $\mathbf{T}_{\text{int}}^{(4)}$, provided by LAMMPS,¹⁰ ensures that $T^{(4)} = (0, T_x, T_y, T_z) = (0, \mathbf{T})$.

Henceforward the matrix index “ 4×4 ” indicates four-by-four matrices. In the above relation we have introduced the orthogonal skew-matrix $\mathbb{S}_{4 \times 4}$, given by

$$\mathbb{S}_{4 \times 4} = \begin{pmatrix} Q_0 & -Q_1 & -Q_2 & -Q_3 \\ Q_1 & Q_0 & -Q_3 & Q_2 \\ Q_2 & Q_3 & Q_0 & -Q_1 \\ Q_3 & -Q_2 & Q_1 & Q_0 \end{pmatrix}; \quad (10)$$

further, $\nabla_{\mathbf{Q}^{(4)}} U$ is the gradient of the potential energy with respect to the unit-quaternion vector $\mathbf{Q}^{(4)}$, or, alternatively, in a component-wise notation $\frac{\partial U}{\partial Q_\nu} = \partial_\nu U$, $\nu = 0, 1, 2, 3$.

Since we are dealing with rigid bodies and explicitly avoid intra-molecular interactions we can neglect $\mathbf{T}_{\text{int}}^{(4)}$ in Eq. (9); further, $\mathbb{S}_{4 \times 4}$ is an orthogonal matrix, thus $\mathbb{S}_{4 \times 4} \mathbb{S}_{4 \times 4}^T = \mathbb{S}_{4 \times 4}^T \mathbb{S}_{4 \times 4} = \mathbb{I}_{4 \times 4}$ where $\mathbb{I}_{4 \times 4}$ is the four dimensional unit matrix. Hence we can rewrite Eq. (9) as

$$\nabla_{\mathbf{Q}^{(4)}} U = -2\mathbb{S}_{4 \times 4} \mathbf{T}^{(4)}, \quad (11)$$

and further express $\partial_i U$ in terms of Eq. (11) using the chain rule

$$\partial_i U = \frac{\partial U}{\partial P_i} = \frac{\partial Q_\nu}{\partial P_i} \frac{\partial U}{\partial Q_\nu} = (\mathbb{Q}_{3 \times 4})_{i\nu} \partial_\nu U \quad i = 1, 2, 3 \quad \text{and} \quad \nu = 0, 1, 2, 3; \quad (12)$$

above we have used the Einstein summation convention. For convenience we have introduced the 3×4 matrix $\mathbb{Q}_{3 \times 4}$ with components $\mathbb{Q}_{i\nu} = \frac{\partial Q_\nu}{\partial P_i}$, or equivalently, $\mathbb{Q}_{3 \times 4} = \left(\frac{\partial Q_0}{\partial \mathbf{P}}, \frac{\partial \mathbf{Q}}{\partial \mathbf{P}} \right)$, with components that – using Eq. (8) – can be written as

$$\frac{\partial Q_0}{\partial \mathbf{P}} = \left(-\frac{1}{2\theta} \sin \frac{\theta}{2} \right) \mathbf{P}, \quad \text{and} \quad (13)$$

$$\frac{\partial \mathbf{Q}}{\partial \mathbf{P}} = \frac{2}{\theta^2} \left(\cos \frac{\theta}{2} - \frac{1}{2\theta} \sin \frac{\theta}{2} \right) \mathbf{P} \cdot \mathbf{P}^T + \left(\theta^2 \sin \frac{\theta}{2} \right) \mathbb{I}; \quad (14)$$

here $\mathbf{Q} = (Q_1, Q_2, Q_3)$, $\mathbf{P} \cdot \mathbf{P}^T = \theta^2 (\tilde{\mathbb{P}}\tilde{\mathbb{P}} + \mathbb{I})$, where \mathbb{I} is again the 3×3 identity matrix, the dot represents a dyadic product, and $\tilde{\mathbb{P}}$ is defined in Eq. (2).

With relation (11) and using $\mathbb{Q}_{i\nu}$, given by Eqs. (13) and (14), we can rewrite Eq. (12)

as

$$\nabla_{\mathbf{P}}U = -2\mathbf{Q}\mathbf{S}T^{(4)} = \mathbb{P}\mathbf{T} \quad (15)$$

with the 3×3 matrix

$$\mathbb{P} = \frac{1}{\theta} \left[(\cos \theta - 1)\mathbb{I} + (\sin \theta - \theta)\tilde{\mathbb{P}} \right] \tilde{\mathbb{P}} - \mathbb{I}, \quad (16)$$

and with $\mathbf{T} = (T_x, T_y, T_z)$ being the torque in Cartesian coordinates in the lab-frame.

3.2 Order parameters

In order to quantify the structural difference between configurations identified via the optimization procedure we associate a feature vector (i.e., a set of order parameters), \mathbf{f} , to every configuration, \mathcal{G} as defined by Eq. (8) of the main text. In this work we mainly rely on the so-called bond orientational order parameters (to be denoted by $\Psi(\nu)$) defined in Refs. 11–13, which provide information about the positional order of ordered structures, and two variants of orientational order parameters (to be denoted by α and β) put forward in Ref. 14 which correlate spatial and orientational degrees of freedom.

The evaluation of local order parameters strongly depends on the method on how to identify neighbors: in this contribution we use the well-defined method of Voronoi construction.^{15,16} Further, the above order parameters are defined for two dimensional systems. In our case of a quasi-two dimensional geometry, with a molecular self-assembly in a plane and with slightly stacked 3D structures, we use for the calculation of the order parameters the projected coordinates of all molecules to the $z = 0$ plane.

All of these order parameters describe global properties (or symmetries) of an ordered structure based on the local proximity of its atomic or molecular entities. To be more precise these parameters can be expressed as a sum over local order parameters ψ_i , calculated for all N particles (or in our case molecules) in the system, i.e.,

$$\Psi(\nu) \sim \sum_{i=1}^N \psi_i(\mathbf{r}_i, \mathbf{r}^{\mathcal{N}_i}; \mathbf{u}_i, \mathbf{u}^{\mathcal{N}_i}; \nu); \quad (17)$$

here the \mathbf{r}_i and \mathbf{u}_i specify the position and the orientation of particle i , while $\mathbf{r}^{\mathcal{N}_i}$ and $\mathbf{u}^{\mathcal{N}_i}$ are the set of positions and orientations of the neighboring particles, respectively; \mathcal{N}_i is the number of neighbors of particle i ; the role of ν will be specified below.

To be more specific: bond orientational order parameters, $\Psi(\nu)$, as defined in Refs. 11,12 and revisited in Ref. 13, depend only on the relative angle, ϕ_{ij} (with $\cos \phi_{ij} = \hat{\mathbf{r}}_{ij} \cdot \hat{\mathbf{e}}_{\text{ref}}$), which is enclosed between the bonds of a central particle, i , and the bonds to each of its \mathcal{N}_i neighbors

$$\Psi(\nu) = \frac{1}{N} \sum_{i=1}^N \left| \frac{1}{\mathcal{N}_i} \sum_{j=1}^{\mathcal{N}_i} \exp[i\nu\phi_{ij}] \right|; \quad (18)$$

here we introduce the vector $\hat{\mathbf{r}}_{ij} = (\mathbf{r}_j - \mathbf{r}_i)/|\mathbf{r}_j - \mathbf{r}_i|$, i. e., the unit vector between two neighbouring particles i and j , the reference axis $\hat{\mathbf{e}}_{\text{ref}}$ (which is of unit length), and the complex unity i , $i^2 = -1$. The orientational symmetry is quantified by the (integer) variable ν : the ν -fold bond orientational order parameter, $\Psi(\nu)$, assumes the value of one if the angles between neighbors are multiples of $2\pi/\nu$ and attains values close to zero for a disordered particle arrangement or if the ν -fold symmetry is not present. However, the lattices we are dealing with are never perfect and the number of nearest neighbors can differ from the ideal value. These issues make the evaluation of bond-orientational order parameters numerically unstable, even for tiny deviations of the particle positions from the ideal configuration.¹⁷ In an effort to guarantee, nevertheless, numerical stability in the evaluations of the $\Psi(\nu)$, we use a modification of the above defined bond orientational order parameter, which was proposed in Ref. 18: this modified definition includes a weighting factor which is related to the polygon side length, l_{ij} , that neighboring particles share

$$\Psi(\nu) = \frac{1}{N} \sum_{i=1}^N \left| \frac{1}{L_i} \sum_{j=1}^{\mathcal{N}_i} l_{ij} \exp[i\nu\phi_{ij}] \right|; \quad (19)$$

with $L_i = \sum_{j=1}^{\mathcal{N}_i} l_{ij}$; the polygon side lengths, l_{ij} , are extracted from the Voronoi construction.

Since the molecules (and hence their interactions) are anisotropic, it is useful to quantify their orientational order. Similar to Eq. (19) we can quantify global *orientational* order including again the above Voronoi nearest-neighbor construction in the following way:

$$\beta = \frac{1}{2N} \sum_{i=1}^N \frac{1}{L_i} \sum_{j=1}^{\mathcal{N}_i} l_{ij} |\hat{\mathbf{u}}_i \cdot \hat{\mathbf{u}}_j|. \quad (20)$$

Finally, we can combine orientational order with positional degrees of freedom, using the unit vector $\hat{\mathbf{r}}_{ij}$ between two neighboring particles i and j :

$$\alpha = \frac{1}{2N} \sum_{i=1}^N \frac{1}{L_i} \sum_{j=1}^{\mathcal{N}_i} l_{ij} |(\hat{\mathbf{u}}_i \cdot \hat{\mathbf{r}}_{ij})^2 + (\hat{\mathbf{u}}_j \cdot \hat{\mathbf{r}}_{ij})^2|, \quad (21)$$

suggesting again a modified version of the order parameters with the side lengths of the Voronoi polygons, l_{ij} ; ¹⁴ $\hat{\mathbf{u}}_i$ is here a unit-vector defining the orientation of a particle in the lab-frame. For a molecule, specified by the index I we evaluate the orientation, $\hat{\mathbf{u}}_I$, by rotating a reference vector, $\hat{\mathbf{e}}_{\text{ref}} = \hat{\mathbf{e}}_x$, according to the current angle-axis vector, \mathbf{P}_I : $\hat{\mathbf{u}}_I = \mathbb{T}(\mathbf{P}_I) \cdot \hat{\mathbf{e}}_{\text{ref}}$ (see Subsection 2.2 of the S.I. for details).

For our PQQP⁺ ClO₄⁻ system we used a set of order parameters to define the feature vector \mathbf{f} :

$$\begin{aligned} \mathbf{f} = & (\Psi_{\text{PQP}}(4), \Psi_{\text{PQP}}(5), \Psi_{\text{PQP}}(6), \\ & \Psi_{\text{ClO}_4}(4), \Psi_{\text{ClO}_4}(5), \Psi_{\text{ClO}_4}(6), \\ & \Psi_{\text{PQP|ClO}_4}(4), \Psi_{\text{PQP|ClO}_4}(5), \Psi_{\text{PQP|ClO}_4}(6), \\ & \beta_{\text{PQP}}, \beta_{\text{ClO}_4}, \\ & \alpha_{\text{PQP}}, \alpha_{\text{ClO}_4}); \end{aligned} \quad (22)$$

here $\Psi_{\text{PQP}}(\nu)$ and $\Psi_{\text{ClO}_4}(\nu)$ quantify the $\nu = 4, 5, 6$ -fold bond-orientational order parame-

ters (see Refs. 11–13), defined by Eq. (19), considering only PQP^+ and ClO_4^- molecules as neighbors. $\Psi_{\text{PQP}|\text{ClO}_4}(\nu)$ quantifies the $\nu = 4, 5, 6$ -fold bond-orientational order parameters for all PQP^+ molecules while considering only ClO_4^- molecules as neighbors. β_{PQP} and β_{ClO_4} , defined by Eq. (20), quantify the orientational-correlation between neighboring PQP^+ and ClO_4^- ions, respectively, while α_{PQP} and α_{ClO_4} , defined by Eq. (21), are in addition sensitive to the respective spatial correlation between neighbours (see Refs. 14,17).

4 Results

4.1 General remarks and system parameters

The following details provide an idea about the numerical costs of our calculations: in order to obtain the ground state configuration for a single state point (specified by a set of the system parameters defined in Subsection 4.1 in the main text) convergence of the full EA+LG ground-state search (based on the evolutionary algorithm (EA) and the local, steepest gradient descent procedure (LG) as specified in Section 3 in the main text) we require at least one to two weeks on one node on the Vienna Scientific Cluster (VSC3) (<http://typo3.vsc.ac.at/systems/vsc-3/>; equipped – per node – with either two Intel Xeon E5-2650v2, 2.6 GHz, eight core processors or two Intel Xeon E5-2660v2, 2.2 GHz, ten core processors from the Ivy Bridge-EP family). We typically used 16 to 20 asynchronous worker processes per evolutionary optimization.

4.2 Clustering of results by similarity

In Subsection 4.2.3 of the main text (see, in particular Fig. 6) we present and discuss results which originate from an independent and separate evolutionary algorithm analysis which focuses entirely on the mobility of the perchlorate anions. This is done by fixing the unit cell as well as the positions and orientations of the contained PQP^+ molecules such that we can study the local minima in the potential energy as a function of the degrees of freedom

of the ClO_4^- molecules. To be more specific these investigations were performed for the structures depicted in Fig. 4(a,e,c) of the main text. Among the solutions identified by the evolutionary algorithm we chose roughly 5000 configurations, all representing a local energy minimum in this energy landscape, for which we evaluated the set of order parameters, \mathbf{f} , specified by Eq.(22) in Subsection 3.2 of the SI. Here we extended this set of order parameters for the problem at hand (i) with additional bond orientational order parameters $\Psi_{\text{ClO}_4}(\nu)$ and $\Psi_{\text{PQP}|\text{ClO}_4}(\nu)$ for $\nu = 3, 8$, and $\Psi_{\text{ClO}_4|\text{PQP}}(\nu)$ for $\nu = 3, 4, 5, 6, 8$, defined analogously to Eqs. (19-22), and (ii) with additional orientational order parameters $\alpha_{\text{ClO}_4|\text{PQP}}$ and $\beta_{\text{ClO}_4|\text{PQP}}$ as defined by Eqs. (20, 21) but considering the orientational order of perchlorate molecules only with respect to PQP^+ neighbors and vice versa, by $\alpha_{\text{PQP}|\text{ClO}_4}$ and $\beta_{\text{PQP}|\text{ClO}_4}$. Further, (iii) we used the minimum, mean, median and maximum value of the z coordinates of all ClO_4^- ions and (iv) the argument of the first peak in the radial distribution function of the perchlorates and (v) of all molecules.

In order to identify configurations which are similar in their structure among all these particle arrangements and to further distinguish between different collections of similar structures in these large sets of data we used unsupervised clustering techniques; a very instructive review on such useful tools and many other helpful machine learning applications in physics or chemistry can be found in Ref. 19.

To be more specific, we combine here the so-called principal component analysis (PCA)²⁰ which reduces the dimensionality of our structural data (or better order parameters thereof) and a successive t-stochastic neighbor embedding (t-SNE)²¹ in order to map high-dimensional data points to low-dimensional embedding coordinates (in two or three dimensions), while preserving the local structure in the data.¹⁹ With this tool at hand we aim at representing high-dimensional data in two or three dimensions in order to unravel hidden – or hard to identify – geometries (such as structural similarities) within the data set.

Coming back to the discussion on the study of the perchlorate molecules we narrowed down the collection of different structures by admitting only such molecular arrangements

whose energy is located within a certain threshold interval, ΔE , above the energy of the related best structures, respectively.

The respective set of order parameters of those structures is first scaled to unit-variance- and zero-mean coordinates considering all data-points. Subsequently, this scaled set is subject to a PCA which is a linear transformation of the F -dimensional data space (in our case of the order parameters or features), \mathbf{f} , to a L -dimensional latent space, $\mathbf{f}' = \mathbf{f} \cdot \mathbb{L}$, using the $F \times L$ projection matrix, \mathbb{L} ; this is done with the intention to identify leading singular values of the correlation matrix of the data which represent directions in the data with large variance, i.e. which contain the most relevant information.¹⁹ Thereby we reduced the number of our order parameters from 32 to five for the results presented in Fig. 6 of the main text.

These five leading principal components, \mathbf{f}' , which exhibit an explained variance above 5%, are then subject to a t-SNE analysis. The idea behind such an analysis is to identify neighbouring data-points (in our case in the latent space after the PCA): this is done by matching the probability distribution $p_{ij} \propto \exp(-|\mathbf{f}'_i - \mathbf{f}'_j|^2 / (2\sigma_i^2))$, which quantifies the likelihood that \mathbf{f}'_j is a neighbour of \mathbf{f}'_i (where σ_i is a bandwidth parameter and is usually determined by fixing the local entropy $H(p_i) = -\sum_j p_{ji} \log_2(p_{ji})$) with a similar probability distribution $q_{ij} \propto (1 + |\mathbf{t}_i - \mathbf{t}_j|^2)^{-1}$ by minimizing the Kullback-Leibler divergence, $D_{\text{KL}}(p||q) = \sum_{ij} p_{ij} \log(p_{ij}/q_{ij}) \rightarrow \min$, between q_{ij} and the symmetrized probability distributions $p_{ij} = (p_{ij} + p_{ji}) / (2N)$; the indices i and j run over the number of data-points. Neighbouring data points with small separations, $|\mathbf{f}'_i - \mathbf{f}'_j|^2$ and $|\mathbf{t}_i - \mathbf{t}_j|^2$, contribute most to p_{ij} and q_{ij} , respectively; however, in contrast to the p_{ij} latent space data-points, \mathbf{t}_i and \mathbf{t}_j , are explicitly encouraged to repel each other if they are far apart by the tails of q_{ij} . This approach can be interpreted as equilibrating the effects of attractive forces acting on neighbouring data-points (being grouped within a cluster) and repulsive forces between whole clusters (separating different groups). Hence, it is easier to visually separate clusters in a few t-SNE dimensions than in a higher dimensional PCA latent space;¹⁹ the results of a two-dimensional t-SNE analysis of our problem at hand can also be observed in Fig. 5. In

addition, we performed a DBSCAN,²² i.e., a density-based clustering algorithm which automatically labels the different clusters; these labels are highlighted in the left panel of this figure by color coding.

The minimum energy of each cluster of structures is indicated in the right panel of this figure by a color code; the results clearly indicate, that several clusters are separated by only minute energy differences. Four of these configurations, separated by an energy difference of 38 meV per molecule pair, are shown in Fig. 6 of the main text.

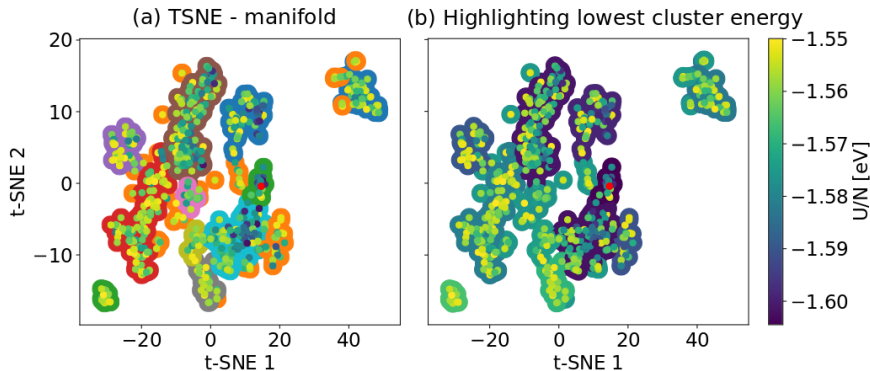


Figure 5: (color online) Dimensional reduction of order parameters into a two dimensional manifold spanned by t -SNE 1 and t -SNE 2 using t-SNE clustering²¹ for the results presented in Fig. 6 of the main text, in order to identify structurally different configurations. (a): separated clusters represent structurally different configurations. The energy of each configurations is color-coded (small dots) and given per $\text{PQP}^+ - \text{ClO}_4^-$ pair, N . Labels of clusters are highlighted using larger, uniformly colored dots in the background. (b): same as left but the background-colors of each configuration indicates the minimal cluster energy. The emphasized red dot indicates the structure with the lowest energy.

References

- (1) Chakrabarti, D.; Wales, D. J. Simulations of rigid bodies in an angle-axis framework. *Appl. Environ. Microbiol.* **2008**, *11*, 1970–1976.
- (2) Chakrabarti, D.; Kusumaatmaja, H.; Rühle, V.; Wales, D. J. Exploring energy land-

- scapes: From molecular to mesoscopic systems. *Phys. Chem. Chem. Phys.* **2014**, *16*, 5014–5025.
- (3) Evans, D. J. On the representation of orientation space. *Mol. Phys.* **1977**, *34*, 317–325.
- (4) Allen, M. P.; Tildesley, D. J. *Computer Simulation of Liquids*; Oxford Science Publ; Clarendon Press, 1989.
- (5) Miller, T. F.; Eleftheriou, M.; Pattnaik, P.; Ndirango, A.; News, D.; Martyna, G. J. Symplectic quaternion scheme for biophysical molecular dynamics. *J. Chem. Phys.* **2002**, *116*, 8649–8659.
- (6) Mie, G. Zur kinetischen Theorie der einatomigen Körper. *Ann. Phys.* **1903**, *316*, 657–697.
- (7) Bader, R. F. W. Atoms in Molecules. *Acc. Chem. Res.* **1985**, *18*, 9–15.
- (8) Tang, W.; Sanville, E.; Henkelman, G. A grid-based Bader analysis algorithm without lattice bias. *21*, 084204.
- (9) Jackson, J. D. *Classical electrodynamics*, 3rd ed.; Wiley: New York, NY, 1999.
- (10) Plimpton, S. Fast Parallel Algorithms for Short – Range Molecular Dynamics. *J. Comput. Phys.* **1995**, *117*, 1–19.
- (11) Strandburg, K. J.; Zollweg, J. A.; Chester, G. V. Bond-angular order in two-dimensional Lennard-Jones and hard-disk systems. *Phys. Rev. B* **1984**, *30*, 2755–2759.
- (12) Strandburg, K. J. Two-dimensional melting. *Rev. Mod. Phys.* **1988**, *60*, 161–207.
- (13) Mazars, M. Bond orientational order parameters in the crystalline phases of the classical Yukawa-Wigner bilayers. *EPL* **2008**, *84*, 55002.

- (14) Georgiou, I. A.; Zihlerl, P.; Kahl, G. Antinematic local order in dendrimer liquids. *EPL* **2014**, *106*, 44004.
- (15) Lejeune Dirichlet, G. Über die Reduction der positiven quadratischen Formen mit drei unbestimmten ganzen Zahlen. *J. Reine Angew. Math.* **1850**, *40*, 209–227.
- (16) Voronoi, G. Nouvelles applications des paramtres continus à la théorie des formes quadratiques. Premier mémoire. Sur quelques propriétés des formes quadratiques positives parfaites. *J. Reine Angew. Math.* **1908**, *133*, 97–178.
- (17) Antlanger, M. Ordered equilibrium structures in systems with long-range interactions. Ph.D. thesis, TU Wien, 2015.
- (18) Mickel, W.; Kapfer, S.; Schröder-Turk, G.; Mecke, K. Shortcomings of the bond orientational order parameters for the analysis of disordered particulate matter. *J. Chem. Phys.* **2013**, *138*.
- (19) Mehta, P.; Bukov, M.; Wang, C.-H.; Day, A. G. R.; Richardson, C.; Fisher, C. K.; Schwab, D. J. A high-bias, low-variance introduction to Machine Learning for physicists. *Phys. Rep.* **2019**, *810*, 1–124.
- (20) Jolliffe, I. *Principal component analysis*; Springer Verlag: New York, 2002.
- (21) Maaten, L. V. D.; Hinton, G. Visualizing Data using t-SNE. *J. Mach. Learn. Res* **2008**, *9*, 2579–2605.
- (22) Ester, M.; Kriegel, H.-P.; Sander, J.; Xu, X. A Density-Based Algorithm for Discovering Clusters in Large Spatial Databases with Noise. Proc. of 2nd International Conference on Knowledge Discovery and. 1996; pp 226–231.